GEO-COAT

DEVELOPMENT OF NOVEL AND COST-EFFECTIVE CORROSION RESISTANT COATINGS
FOR HIGH TEMPERATURE GEOTHERMAL APPLICATIONS

Project acronym:	**Geo-Coat**			
Project title:	Development of Novel and Cost-Effective Corrosion Resistant Coatings for High Temperature Geothermal Applications			
Activity:	LCE-07-17-Renewables			
Call:	H2020-LCE-2017-RES-RIA-TwoStage			
Funding Scheme:	RIA	**Grant Agreement:**	LCE-GA-2018-764086	
Project dates:	01/02/2018 – 31/01/2021		**Duration in months:**	36
WP3	**Coating synthesis through thermal spray and laser cladding**			

D3.5: Influence of passive film on the corrosion behaviour of the HEA coating

Due date:	31/03/2019 (M14)	
Actual Submission Date:	29/03/2019	
Lead Beneficiary:	SC TEHNOID COM SRL	
Main authors/contributors:	TEH, MET, UPB, TWI	
Dissemination Level[1]:	PU	
Nature:	Report	
Status of this version:		**Draft under Development**
		For Review by Coordinator
	X	**Submitted**
Version:	02	

REVISION HISTORY

Version	Date	Main Authors/Contributors	Description of changes
02	31/07/2019	TEH, MET, UPB, TWI	Content added with latest technical information

Funded by the Horizon 2020 Framework Programme of the European Union

[1] Dissemination level security:

PU – Public (e.g. on website, for publication etc.) / **PP** – Restricted to other programme participants (incl. Commission services) /

RE – Restricted to a group specified by the consortium (incl. Commission services) / **CO** – confidential, only for members of the consortium (incl. Commission services)

This project has received funding from the European Union's Eighth Framework Programme for research, technological development and demonstration under Grant Agreement No. LCE-GA-2018-764086. This publication reflects the views only of the author(s), and the Commission cannot be held responsible for any use which may be made of the information contained therein.

Copyright © 2018-2021, Geo-Coat Consortium

This document and its contents remain the property of the beneficiaries of the Geo-Coat Consortium and may not be distributed or reproduced without the expressed written approval of the Geo-Coat Coordinator, TWI Ltd. (www.twi-global.com)

THIS DOCUMENT IS PROVIDED BY THE COPYRIGHT HOLDERS AND CONTRIBUTORS "AS IS" AND ANY EXPRESS OR IMPLIED WARRANTIES, INCLUDING, BUT NOT LIMITED TO, THE IMPLIED WARRANTIES OF MERCHANTABILITY AND FITNESS FOR A PARTICULAR PURPOSE ARE DISCLAIMED. IN NO EVENT SHALL THE COPYRIGHT OWNER OR CONTRIBUTORS BE LIABLE FOR ANY DIRECT, INDIRECT, INCIDENTAL, SPECIAL, EXEMPLARY, OR CONSEQUENTIAL DAMAGES (INCLUDING, BUT NOT LIMITED TO, PROCUREMENT OF SUBSTITUTE GOODS OR SERVICES; LOSS OF USE, DATA, OR PROFITS; OR BUSINESS INTERRUPTION) HOWEVER CAUSED AND ON ANY THEORY OF LIABILITY, WHETHER IN CONTRACT, STRICT LIABILITY, OR TORT (INCLUDING NEGLIGENCE OR OTHERWISE) ARISING IN ANY WAY OUT OF THE USE OF THIS DOCUMENT, EVEN IF ADVISED OF THE POSSIBILITY OF SUCH DAMAGE.

SUMMARY

In this deliverable, we present a scientific study on the effect of passive film and heat treatment on the corrosion behaviour of coatings of high-entropy alloys (HEA) deposited through High velocity oxygen-fuel (HVOF) and laser cladding. The corrosion behaviour of HEAs is in fact expected to possess a close relationship with the properties of the passive films. The overall study of this effect is the objective of two deliverables within the Geo-Coat project: the present one and deliverable D3.6 (phase transformation rules to apply heat treatment during the HEA coating synthesis). While deliverable D3.6 focuses on the phase transformations and their effect onto the corrosion resistance of the coatings, this deliverable concentrates on the effect of passive film properties onto the corrosion resistance. To this scope, coated samples were heat-treated, at two levels, in an argon atmosphere. The heat treatment was followed by an electrochemical corrosion process. In this way, both non heat-treated and heat-treated specimens of the same coating material have been tested. For the aspect of the comprehensive characterization of corrosion behaviour, high-resolution observation of the oxide film formation has been be carried out after corrosion testing in both heat-treated and non-heat-treated coatings. The high-resolution investigation, performed through in-situ transmission electron microscopy (TEM), scanning transmission electron microscopy (STEM) and depth-profile studies of passive films will provide an atomistic understanding and is a prerequisite for the control of electrochemical surface processes. The process parameters used to deposit the coatings in this stage have been previously optimised within the project, as described within deliverables D3.2 (report on optimisation of HVOF process for HEA and cermet alloy based coating synthesis) and D3.3 (report on optimisation of laser cladding process for HEA based coating synthesis).

OBJECTIVES MET

The following objectives have been met:

- To study and categorise the chemistry/physics of the HEA passive films and the effects of heat treatment and consolidation on the density and porosity, hence corrosion and erosion resistance, of HEA coatings.

Contents

SUMMARY 5

1. MATERIALS AND SETUP 7

2. METHODOLOGY 9

3. RESULTS AND DISCUSSION 11

3.1 PERFORMANCE AND CHARACTERISATION OF HEAT-TREATED COATINGS 11

3.2 PASSIVE FILM CHARACTERISATION 16

3.2.1 HVOF coatings 17

3.2.1.1 Sample HVOF-HEA2 (non heat-treated)

3.2.1.2 Sample HVOF-HEA2-HT2

3.2.2 Laser cladding coatings 31

3.2.2.1 Sample LC-HEA2 (non heat-treated)

3.2.2.2 Sample LC-HEA2-HT2

4. CONCLUSIONS 42

REFERENCES 42

1. MATERIALS AND SETUP

Within this section we report details of the materials and setup employed for the experiments performed in this stage.

The powders used to produce the coatings in this section are custom made high-entropy alloys (HEA) produced by either mechanical alloying or gas atomisation: HEA 1 – $CoCrFeNiMo_{0.85}$, HEA 3 – CoCrFeNiMo, HEA 4 – $Co_{0.5}CrFeNiMo$, HEA 5 – $Al_{0.5}CoCrFeNi$. An additional powder, HEA 6, has also been produced during the project and although not used for the experiments in this section, it will be analysed at a later stage during the project. A detail on their production methodology and final microstructure has been reported in deliverable D3.2. (Report on optimisation of HVOF process for HEA and cermet alloy based coating synthesis) and D3.6 (Phase transformation rules to apply heat treatment during the HEA coating synthesis) however, a summary of the powders employed is reported in Tab. 1.

Table 1: Powders employed to produce the coatings in this stage.

Powder acronym	Composition	Production process
HEA 1	$CoCrFeNiMo_{0.85}$	Mechanical alloying
HEA 2	$CoCrFeNiMo_{0.85}$	Gas atomisation
HEA 3	CoCrFeNiMo	Mechanical alloying
HEA 4	$Co_{0.5}CrFeNiMo$	Mechanical alloying
HEA 5	$Al_{0.5}CoCrFeNi$	Mechanical alloying

As also described in deliverable D3.6, one set of deposition process parameters has been employed to produce the coatings as a result of the optimisation stage. This optimum set of process parameters (one per powder) has been employed to produce the specimens in this stage by only employing either carbon steel (substrate S1 within Geo-Coat for laser cladding specimens) or stainless steel (substrate S4 within Geo-Coat for HVOF specimens) as substrates of dimensions 25x25x6 mm. Details on powders, deposition process parameters optimisation and setup used for HVOF and laser cladding are presented in deliverables D3.2 (for HVOF) and D3.3 (for laser cladding).

The furnace employed for the heat-treatment runs in this stage is an L laboratory chamber furnace (LAC®), capable of operating in Ar atmosphere up to a temperature of 1200 ^{o}C (Fig. 1).

Figure 1: Furnace used for heat treatment of the HEA coated samples

A Field Emission Scanning Electron Microscope (SEM Supra 25, Zeiss®), equipped with X-Ray Energy Dispersive Spectroscopy (EDS, Oxford instruments®) was employed to evaluate the coatings microstructure. For these analyses, the specimens were cross-sectioned and mounted in a thermosetting phenol formaldehyde resin (Bakelite) and ground and polished with SiC abrasive paper. X-ray Diffraction data for phase characterisation of both powders and coatings has been collected by using a Bruker D8 advance instrument equipped with a Cu target X-ray tube and a diffracted beam monochromator limiting the beam to Cu Kα radiation. Data was collected between $2\theta = 15^{o}$ and 90^{o} at 0.05^{o} intervals. The corrosion performance of both as sprayed and heat-treated coatings has been examined in a 3.5% NaCl aqueous solution at room temperature (25 ^{o}C) and constant pH = 4. The pH was controlled by means of an HCl 7.5M solution during the experiments. Saturated calomel electrode (SCE) and platinated titanium electrode have been used as reference and auxiliary (counter) electrode respectively. Specimens for corrosion experiments were tested in the as-deposited or as-heat-treated condition and sealed using epoxy resin, leaving an area of approximately 1 cm^2 exposed to the solution. The experimental setup of the electrochemical corrosion apparatus was in compliance with ASTM G5-14, ASTM G59-97. The electrochemical properties of the specimens were assessed experimentally by potentiodynamic polarisation resistance and Tafel scan measurements following ASTM G102-89. All potentiodynamic polarisation measurements were taken using an ACM Instruments® Gill 16 electrochemical system while a Bank Elektronik Gmbh® Azelle 5 avesta cell was employed for the Tafel scans. Potentiodynamic polarisation measurements were taken at -/+ 10 mV versus the corrosion potential, with a scanning rate of 10 mV/min and a total testing time of 1 week. The current density values were normalised to the exposed surface area. Tafel scan measurements were taken from -250 mV to + 150 mV versus open-circuit potential (E_{OCP}) at a scanning rate of 0.5 mV/s by first keeping the working electrode immersed into the test solution at E_{OCP} for 60 min to attain a steady-state condition. Results were analysed by using the ACM® Core Running software. An in depth description of the electrochemical equipment is provided in deliverable D5.3 (Ranking of the synthesised coatings). After electrochemical corrosion the samples have been analysed through transmission electron microscopy (TEM) and scanning transmission electron microscopy (STEM), Energy dispersive X-ray spectroscopy (EDX) and electron energy loss spectroscopy (EELS), all performed with the Tecnai® G2 F30S-TWIN Quanta equipment (Fig. 2). For TEM lamella preparation, the Ultracut Ultramicrotome

Leica® EM UC7 has been employed equipped with a micro-diamond knife, followed by a low angle ion milling & polishing system Model 1010 (Fischione®) for lamella thickness refinement.

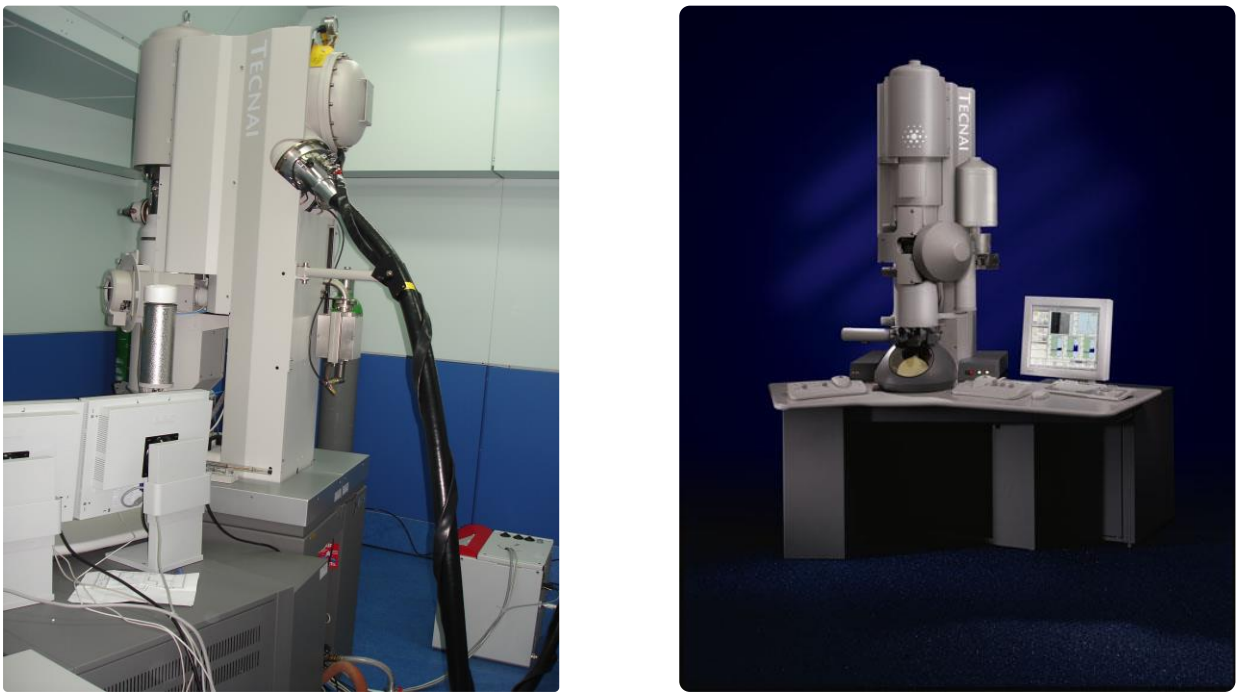

Figure 2: The METAV TEM equipment - Tecnai G2 F30S-TWIN Quanta, equipped with energy-dispersive x-ray spectroscopy (EDX) and electron energy-loss spectroscopy (EELS)

2. METHODOLOGY

The deposition process parameters employed, for each of the powders in Tab. 1 (except HEA 6), to deposit the coatings for this report are the optimised ones as described within deliverables D3.2 (for HVOF) and D3.3 (for laser cladding). In this stage, for each material, three types of specimens have been tested for corrosion: one in the as-deposited condition, one in the as-deposited plus heat-treated at condition HT_1 and finally one in the as-deposited plus heat-treated at condition HT_2. Details of these two heat treatments are reported in Tab. 2. Both heat treatments are composed of two steps: a first dwell at 500 ^{o}C for 60 min for both HT_1 and HT_2, aimed at relieving the residual stresses within the coatings and a second dwell, at two different temperatures in the two cases: 900 ^{o}C and 1100 ^{o}C for HT_1 and HT_2 respectively, in both cases for 60 min. These higher temperatures were selected to impact the coating microstructure and increase the bonding between the substrate and the coated layer by enhancing interdiffusion mechanisms. Argon was flushed during the tests and a natural cooling was employed at the end of the cycle to take the specimens down to room temperature.

Table 2: The two sets of heat treatment parameters (HT_1 and HT_2) used for the experiments.

Heat treatment	**T1** (^{o}C)	**HR1** (^{o}C/min)	**t1** (min)	**T2** (^{o}C)	**HR2** (^{o}C/min)	**T2** (min)	**Cooling type**
HT_1	500	10	60	900	10	60	Natural furnace atmosphere
HT_2	500	10	60	1100	10	60	Natural furnace atmosphere

As a result, the overall number of specimens produced by heat treatment is reported in Tab. 3. Notice that these are the same specimens as produced for deliverable D3.6. It is worth noting that no HVOF-HEA5 specimens have been produced as this has not been deemed appropriate for further analysis from microstructural analysis (see deliverable D3.2).

Table 3: Summary of specimens processed for this study

Specimen name	Deposition technique	Heat treatment type
HVOF_HEA1_HT1	HVOF	HT_1
HVOF_HEA1_HT2	HVOF	HT_2
HVOF_HEA2_HT1	HVOF	HT_1
HVOF_HEA1_HT2	HVOF	HT_2
HVOF_HEA3_HT1	HVOF	HT_1
HVOF_HEA3_HT2	HVOF	HT_2
HVOF_HEA4_HT1	HVOF	HT_1
HVOF_HEA4_HT2	HVOF	HT_2
LC_HEA1_HT1	Laser cladding	HT_1
LC_HEA1_HT2	Laser cladding	HT_2
LC_HEA2_HT1	Laser cladding	HT_1
LC_HEA1_HT2	Laser cladding	HT_2
LC _HEA3_HT1	Laser cladding	HT_1
LC_HEA3_HT2	Laser cladding	HT_2
LC_HEA4_HT1	Laser cladding	HT_1
LC_HEA4_HT2	Laser cladding	HT_2
LC_HEA5_HT1	Laser cladding	HT_1
LC_HEA5_HT2	Laser cladding	HT_2

The coatings so produced have been tested for corrosion performance. After electrochemical corrosion the samples are analysed through transmission electron microscopy (TEM) and scanning transmission electron microscopy (STEM), Energy dispersive X-ray spectroscopy (EDX) and electron energy loss spectroscopy (EELS).Lamellas for TEM analysis were prepared by using the following procedure:

1. Mechanically section (cleave, saw) the sample.
2. Ultrasonically cut disks (3 mm diameter by <500 μm thick).
3. Rough grind (3 mm diameter by <75 μm thick).
4. Dimple grind (3 mm diameter by <10 μm center thickness).
5. Ion mill the top and bottom surfaces until they are electron transparent (3 mm diameter by <100 nm thickness).
6. Plasma cleaning.

3. RESULTS AND DISCUSSION

3.1 PERFORMANCE AND CHARACTERISATION OF HEAT-TREATED COATINGS

Photographs of the corroded surface of each specimen is reported in Tab. 4. Coatings corresponding to the same powder material and technique are reported on the same row, with the different heat treatments reported in subsequent columns.

Table 4: Surface photographs of HVOF and LC coated samples

HVOF - HEA1 – S4	HVOF - HEA1 – S4 – HT1	HVOF - HEA1 – S4 – HT2
		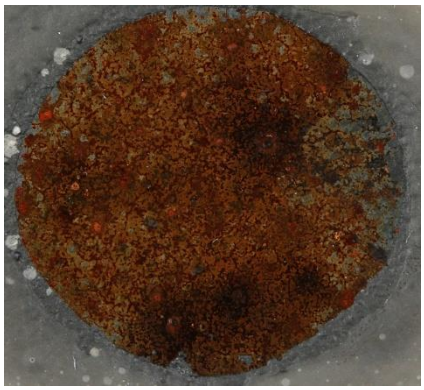
HVOF - HEA2 – S1	HVOF - HEA2 – S1 – HT1	HVOF - HEA2 – S1 – HT2
	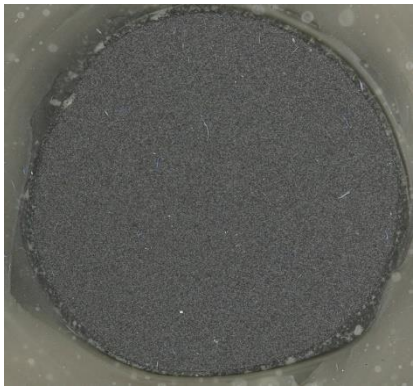	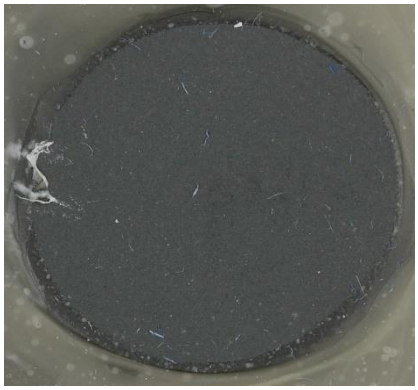
HVOF - HEA3 – S4	HVOF - HEA3 – S4 – HT1	HVOF - HEA3 – S4 – HT2
	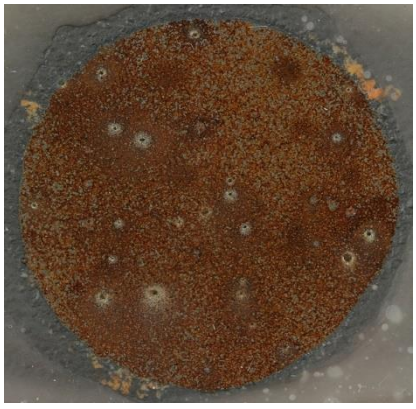	coating flaked off during preparation
HVOF - HEA4 – S4	HVOF - HEA4 – S4 – HT1	HVOF - HEA4 – S4 – HT2

		coating flaked off during preparation
LC - HEA1 – S1	LC - HEA1 – S1 –HT1	LC - HEA1 – S1 –HT2
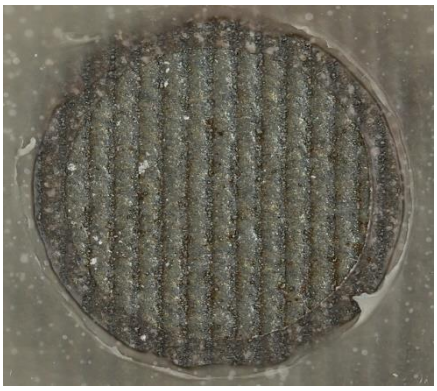	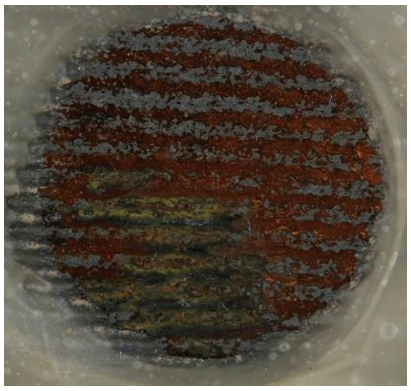	
LC – HEA2 – S1	LC – HEA2 – S1 –HT1	LC – HEA2 – S1 –HT2
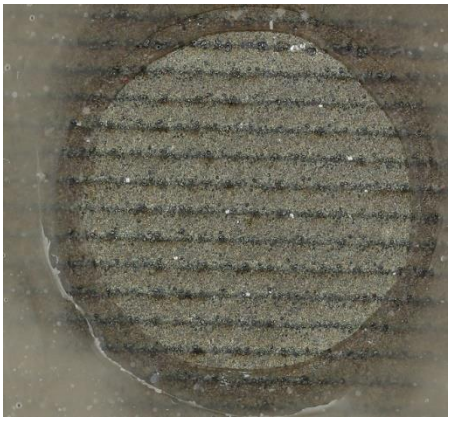		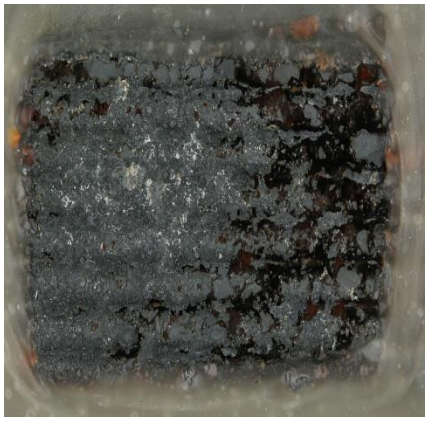
LC – HEA3 – S1	LC – HEA3 – S1 –HT1	LC – HEA3 – S1 –HT2
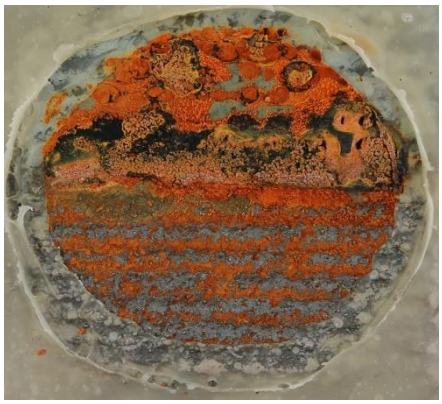	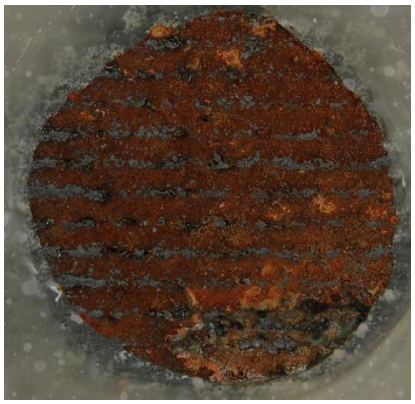	
LC – HEA4 - S1	LC – HEA4 – S1 –HT1	LC – HEA4 – S1 –HT2

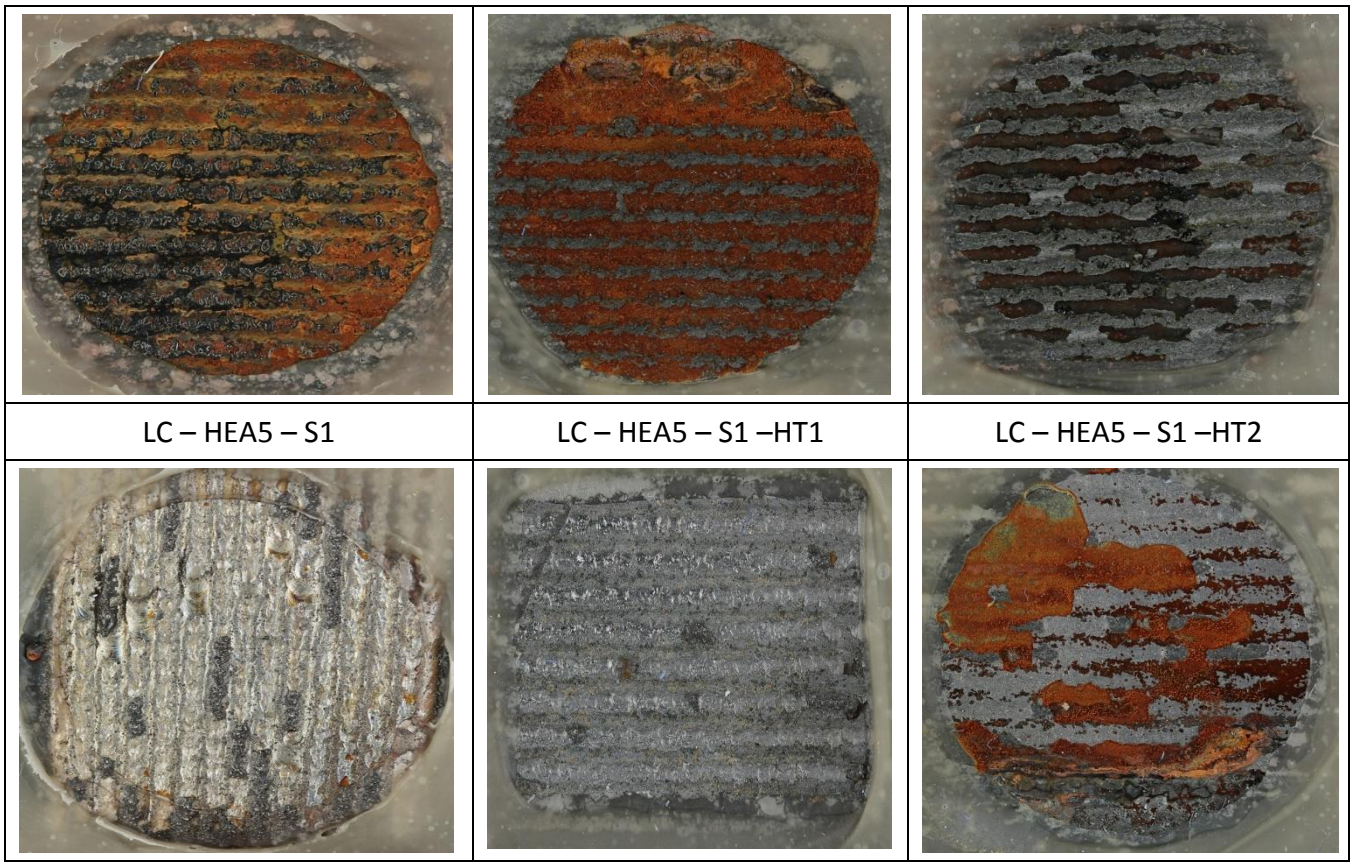

As it can be seen from the photographs, two of the specimens, HVOF-HEA3-S4-HT2 and HVOF-HEA4-S4-HT2 could not be tested as the coating flaked off during the preparation operations for electrochemical testing. This is likely due to build-up of stress during the heating cycle due to the difference in coefficient of thermal expansion (CTE) between the deposited coating and substrate. This demonstrates the poor adhesion properties of these two coatings and it has therefore been decided to not further proceed with their analysis. It is worth nothing how a clear improvement in corrosion properties is only observed for specimen HVOF-HEA2, while no clear conclusions can be deduced after visual observation. The corrosion rates calculated for the specimens tested are reported in Table 5 and a visual representation is reported in Figures 3 and 4.

Table 5: Corrosion rate results for the all the specimens tested in this stage.

Specimen name	Substrate	Powder	Technique	Corrosion rate [mm/yr]
HVOF - HEA1 – S4	S4	HEA1	HVOF	0.48
HVOF - HEA1 – S4 – HT1	S4	HEA1	HVOF	0.55
HVOF - HEA1 – S4 – HT2	S4	HEA1	HVOF	0.56
HVOF - HEA2 – S1	S1	HEA2	HVOF	0.78
HVOF - HEA2 – S1 – HT1	S1	HEA2	HVOF	0.063
HVOF - HEA2 – S1 – HT2	S1	HEA2	HVOF	0.036
HVOF - HEA3 – S4	S4	HEA3	HVOF	0.75
HVOF - HEA3 – S4 – HT1	S4	HEA3	HVOF	0.44
HVOF - HEA3 – S4 – HT2*	S4	HEA3	HVOF	Unknown/coating flaked off

HVOF - HEA4 – S4	S4	HEA4	HVOF	0.64
HVOF - HEA4 – S4 – HT1	S4	HEA4	HVOF	0.37
HVOF - HEA4 – S4 – HT2*	S4	HEA4	HVOF	Unknown/coating flaked off
LC - HEA1 – S1	S1	HEA1	LC	0.038
LC - HEA1 – S1 –HT1	S1	HEA1	LC	0.997
LC - HEA1 – S1 –HT2	S1	HEA1	LC	1.66
LC – HEA2 – S1	S1	HEA2	LC	0.00144
LC – HEA2 – S1 –HT1	S1	HEA2	LC	0.25
LC – HEA2 – S1 –HT2	S1	HEA2	LC	1.49
LC – HEA3 – S1	S1	HEA3	LC	0.032
LC – HEA3 – S1 –HT1	S1	HEA3	LC	0.93
LC – HEA3 – S1 –HT2	S1	HEA3	LC	0.84
LC – HEA4 - S1	S1	HEA4	LC	0.034
LC – HEA4 – S1 –HT1	S1	HEA4	LC	1.497
LC – HEA4 – S1 –HT2	S1	HEA4	LC	1.58
LC – HEA5 – S1	S1	HEA5	LC	0.0095
LC – HEA5 – S1 –HT1	S1	HEA5	LC	0.13
LC – HEA5 – S1 –HT2	S1	HEA5	LC	0.47

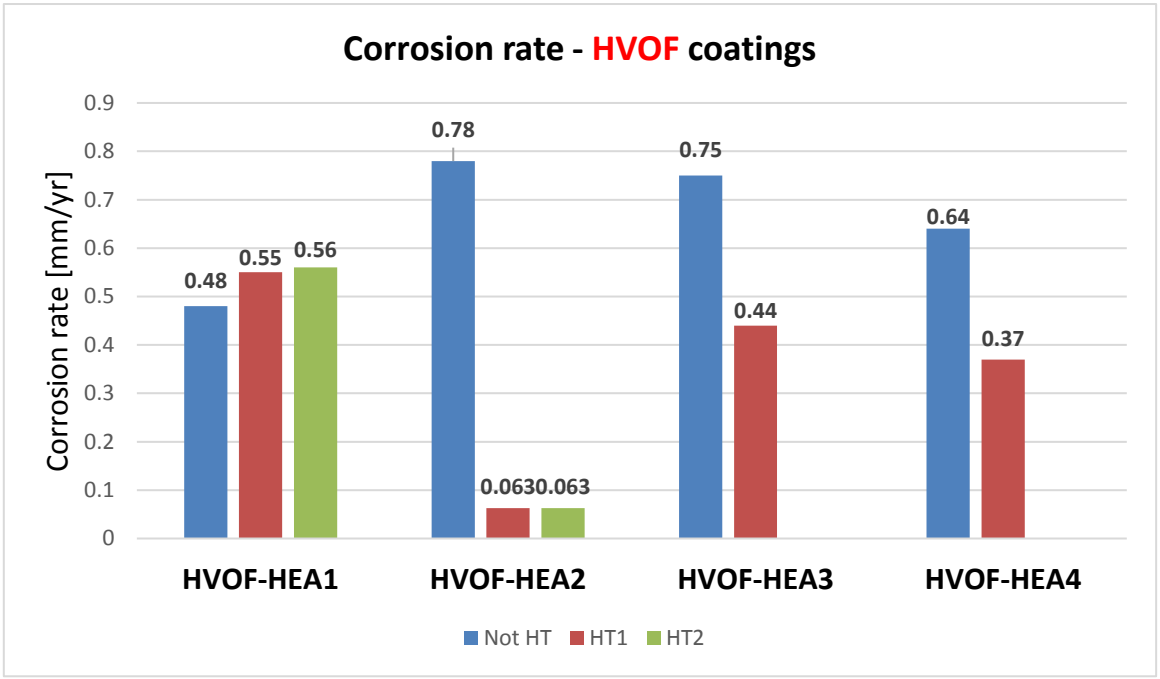

Figure 3: Corrosion rate results for HVOF coated samples

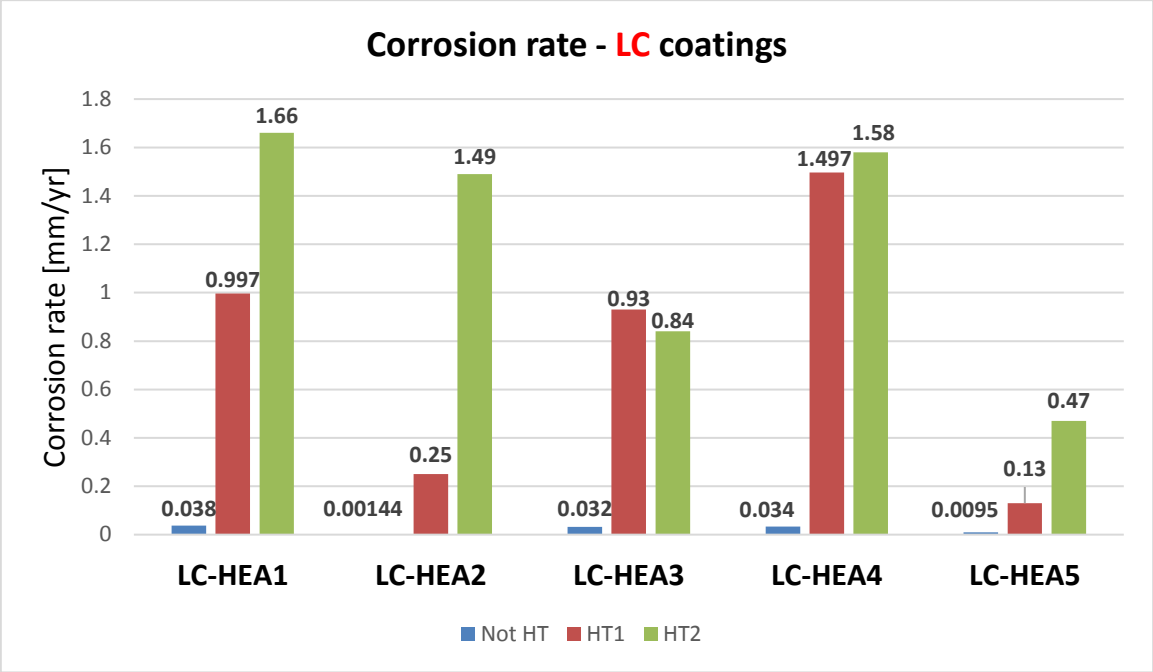

Figure 4: Corrosion rate results for the LC coated samples.

Apart from powder HEA1, the HVOF coatings (when not delaminated as in the case of HVOF-HEA3-HT2 and HVOF-HEA4-HT2) generally seem to benefit from the heat treatment. The main effect is measured in specimen HVOF-HEA2 where a decrease of one order of magnitude is measured in the heat-treated coatings compared to the as-deposited ones. Moreover, the corrosion rate of specimen HVOF-HEA2-HT1 results one order of magnitude lower than the lowest value measured on non-heat-treated specimens (i.e. HVOF-HEA1). The opposite trend is instead measured in the laser cladded (LC) coatings, where a decrease in corrosion rate is observed in all the heat-treated specimens compared to the respective as-deposited ones. The highest corrosion rate after heat treatment is measured, in almost all cases except specimen LC-HEA3, on specimens treated at the higher temperature among the two tested, i.e. HT2. The difference between corrosion rates pre-and post-heat-treatment is significant as it lies in the two orders of magnitude difference for most LC coatings. It is worth noting however, that care must be taken when interpreting the above results as through-coating permeation has been previously observed, from work performed in the project, on non-heat-treated specimens HEA1, HEA3 and HEA4 (HVOF) and HEA3 and HEA4 (LC). If permeation has occurred, the corrosions rate results would be affected by exposure of the substrate as well as the coating, which would make the corrosion rate value not only related to the coating.

3.2 PASSIVE FILM CHARACTERISATION

Significant work has been performed, within the last decade, on developing corrosion-resistant HEA alloys [1]. The exceptional corrosion performance measured on these systems, even superior to conventional alloys, has been owed to the presence of passivating elements, such as Cr, Ni, Mo, etc. In chloride-containing solutions, such as the one employed in this work, the mechanism of corrosion is driven by detrimental Cl^- anions, that can absorb on the surface of the passive layer and then penetrate through the oxide film. The success of a passive layer in hindering corrosion phenomena is therefore determined by the type and distribution of alloying elements on the surface of the alloy in contact with the solution. The effect of addition of different elements, such as Al, Cu and Mo has on

the corrosion behaviour of bulk and coatings HEAs has been extensively studied with different results in terms of improvement/worsening of the overall behaviour [1].

With regards to the effect of heat treatment onto the corrosion performance of HEA systems, it can be assumed, as a general rule, that an increase in temperature would enhance the formation of a solid solution phase against intermetallic compounds (deleterious for corrosion performance) following the Gibbs free-energy rule $\Delta G=\Delta H-T\Delta S$. However, it has been demonstrated that care must be taken in designing the heat-treatment temperature profiles in order to avoid the formation of undesired phases [1].

In this paragraph, an attempt will be made in explaining the corrosion rate results obtained, by selecting two systems (Table 6):

1. A system where an **improvement** in corrosion performance is observed after heat-treatment, HVOF-HEA2,
2. A system where a **decrease** in corrosion performance is observed after heat treatment, LC-HEA2.

Table 6: Specimens selected for future SEM and TEM investigations

Specimen name	Substrate	Powder	Technique	Corrosion rate (mm/yr)
HVOF - HEA2 – S1	S1	HEA2	HVOF	0.78
HVOF - HEA2 – S1 – HT2	S1	HEA2	HVOF	0.036
LC – HEA2 – S1	S1	HEA2	LC	0.00144
LC – HEA2 – S1 –HT2	S1	HEA2	LC	1.49

The selected systems, all deposited onto substrate S1, have been analysed, after exposure, by means of SEM-EDX and TEM analysis.

3.2.1 HVOF COATINGS

3.2.1.1 Sample HVOF-HEA2-S1 (non heat-treated)

A photograph of the mounted cross-section of specimen HVOF-HEA2-S1 (non heat-treated) is depicted in Figure 8.

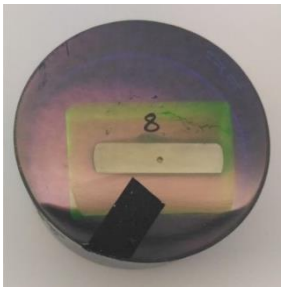

Figure 8: Cross-section through the HVOF-HEA2-S1 specimen for microstructural analysis.

The corresponding SEM micrographs are reported in Figure 9 at low (a) and high magnification (b).

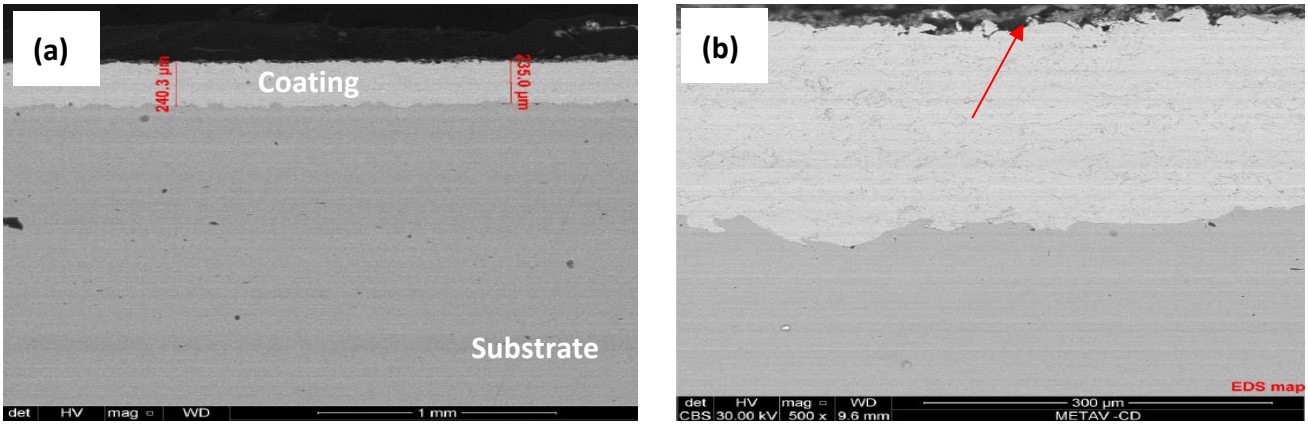

Figure 9: SEM micrographs showing the HEA deposition sample in cross section and the interface of the specimen at (a) low and (b) high magnification.

The coatings exhibit a uniform microstructure and a low presence of defects (i.e. pores and cracks). The interface with the substrate also seems quite uniform with no visible delamination observed. A product of darker colour seems to be visible on the surface of the coating, as indicated by the red arrow in Figure 9 (b). Insights into the nature of this layer can be found by EDX analysis of the region in Figure 9 (b), as depicted in Figure 10.

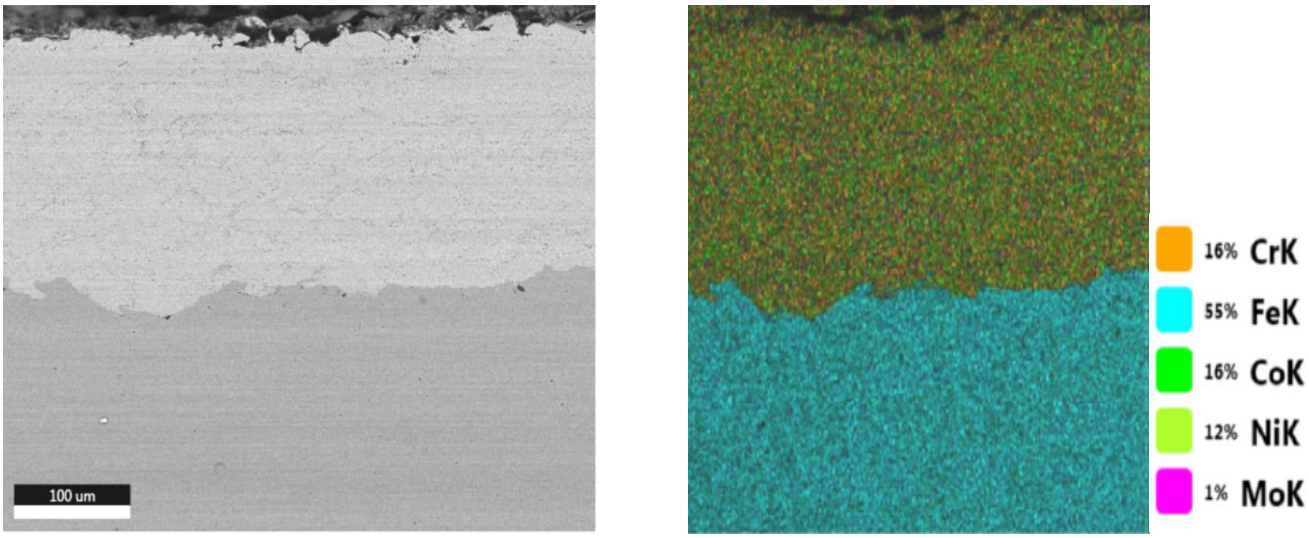

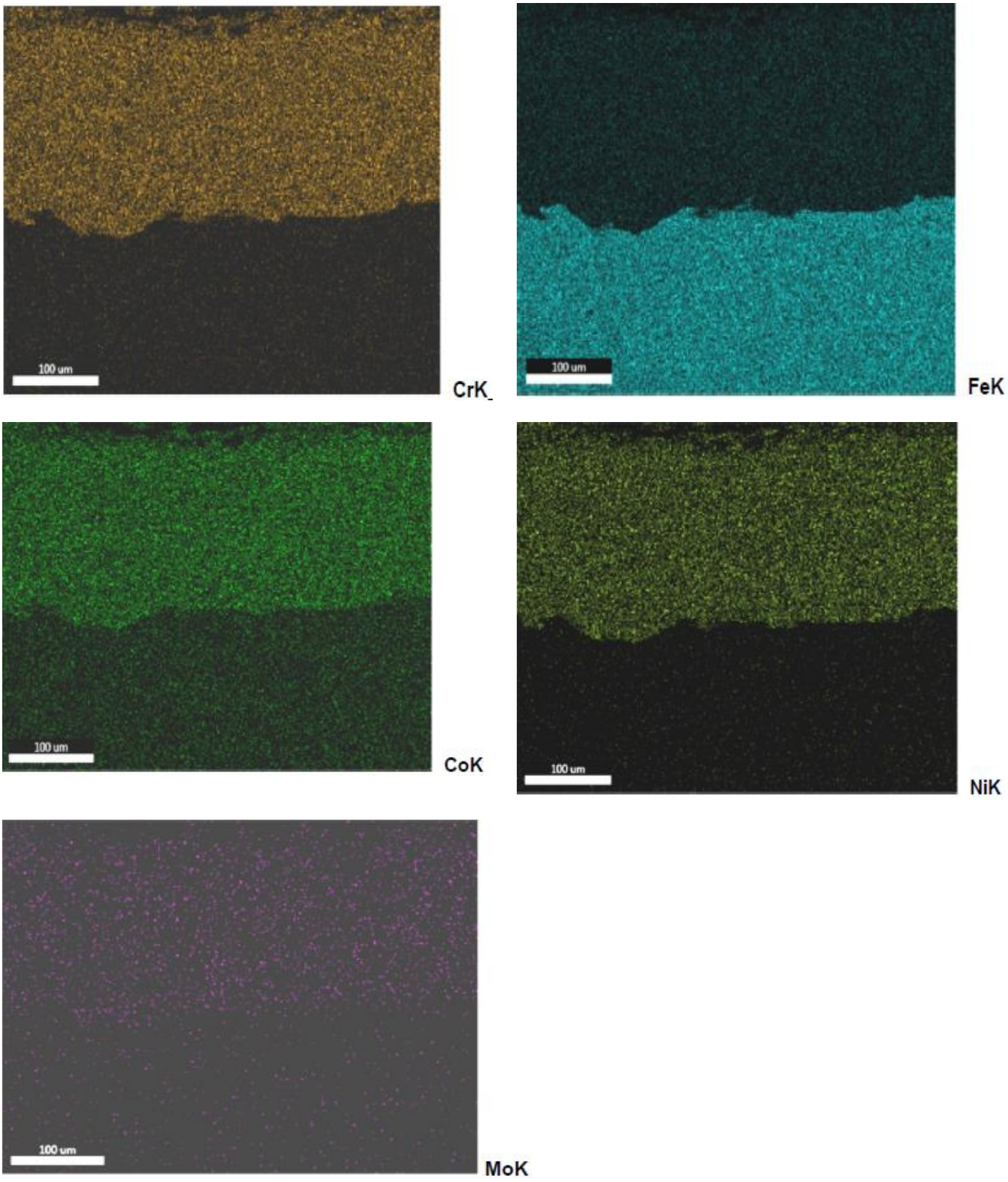

Figure 10: SEM and EDX general analysis showing X-ray mapping for HEA elements and identification of disperse deposition of elements.

The EDX analysis seems to reveal that the scale layer on top of the coating contains all of the HEA components: Co, Cr, Fe, Mo and Ni with no clear dominance indication. In order to further investigate the properties of the top layer, TEM analysis has been performed on a region at the surface of the coating (Figure 11).

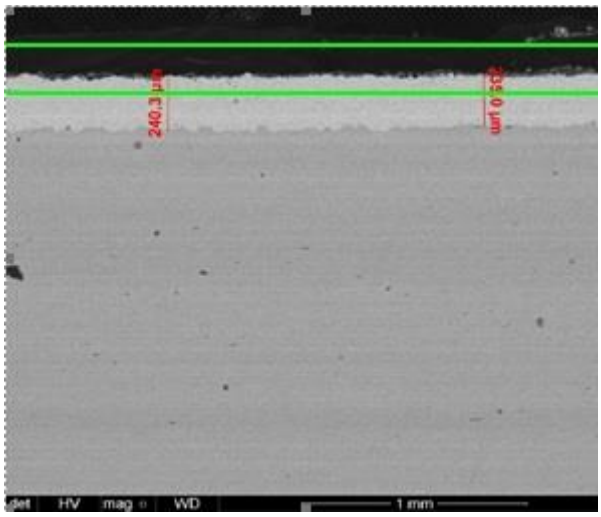

Figure 11: SEM micrograph showing the HEA deposition sample in the cross-section and indication of the area for TEM sample preparation in green.

Results from the TEM analysis are reported in Figure 12. The figure shows a typical HEA structure observed after HEA coating deposition. Micro-precipitates are clearly observed, as denoted by areas of different intensity.

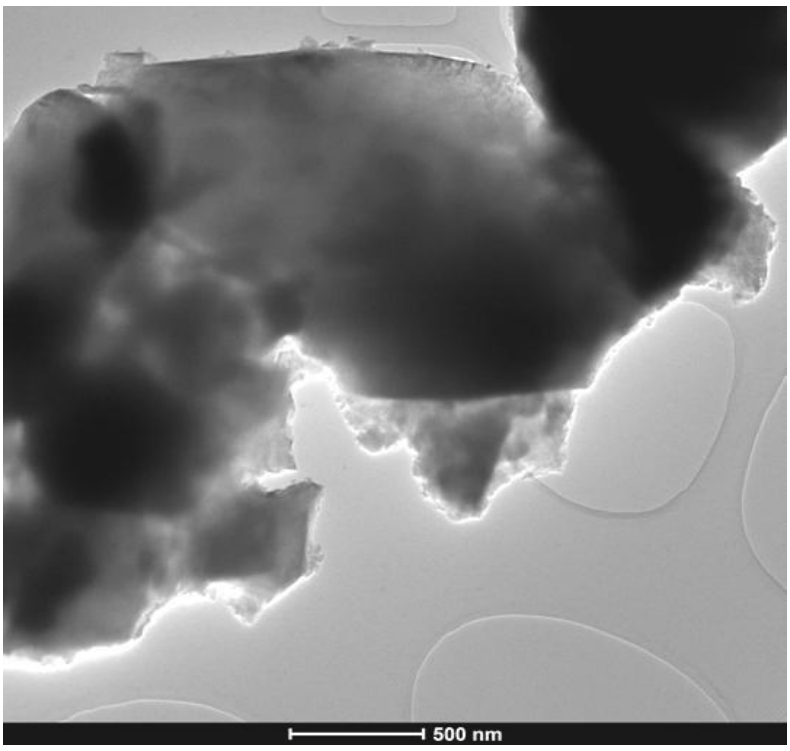

Figure 12: TEM micrograph of HVOF-HEA2 coating. The HEA alloy forming some micro constituent in specific areas.

A more detailed analysis has been performed, as seen by the high-magnification micrograph in Figure 13. Analysis shows that all of the elements within the HEA composition: Ni, Co, Mo and Fe components are identified within the region, as also demonstrated by EDX analysis (Figure 14). However, the prevalence of the Cr element, together with oxygen, suggests the formation of chromium-rich oxides.

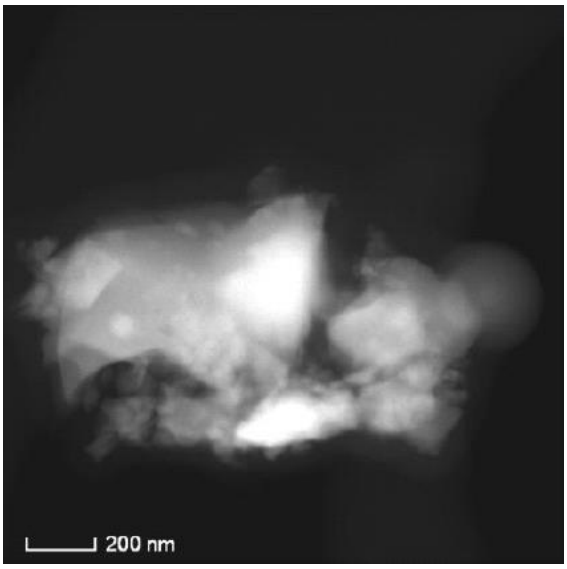

Figure 13: TEM micrographs of surface region of specimen HVOF-HEA2 (non heat-treated). The micro-precipitates have been identified as Ni-Co-Mo-Fe.

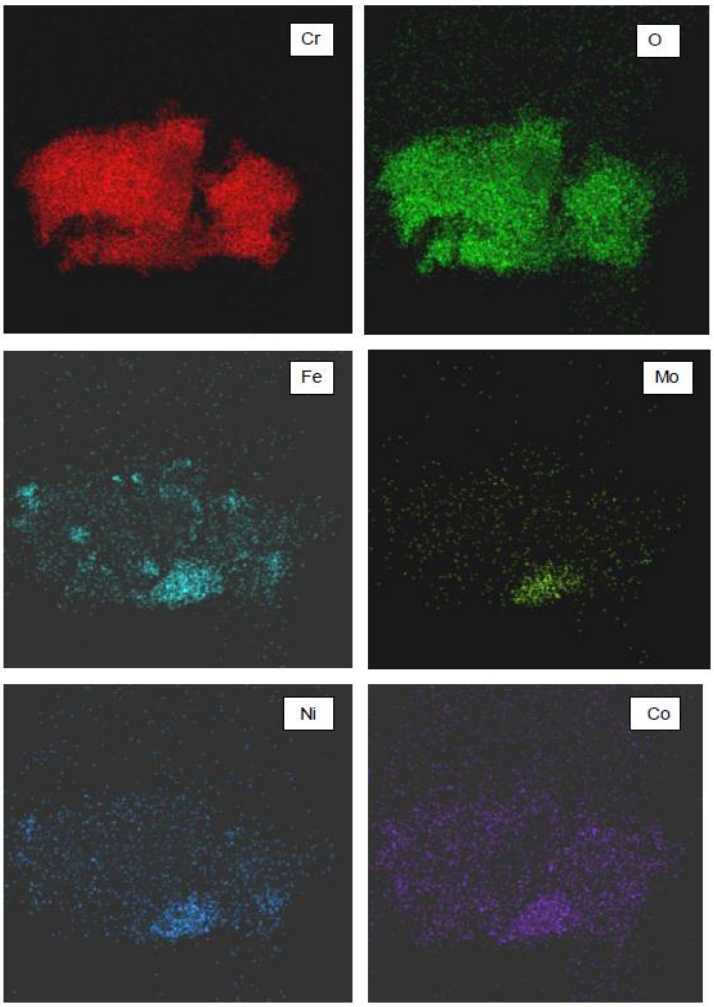

Figure 14: TEM mapping of HEA specimen showing the element distributions. Note a local area distribution of Mo particle with complex HEA matrix.

Figure 14 also suggests the limited presence of the Mo component in the region. This could be due to either formation of soluble Mo products or the thermodynamic preference for the formation of Cr-based oxides over Mo ones.

Detailed HRTEM images of the microstructure of the samples under investigation are shown in Figure 15 and Figure 16. The surface layer of sample is polycrystalline and its thickness is of about 100-500nm, representing HEA precipitates and chromium oxide embedded in it. Crystalline domain with different orientations, denoted with N are clear identification. As a rule the crystalline grain are with non-regular shape.

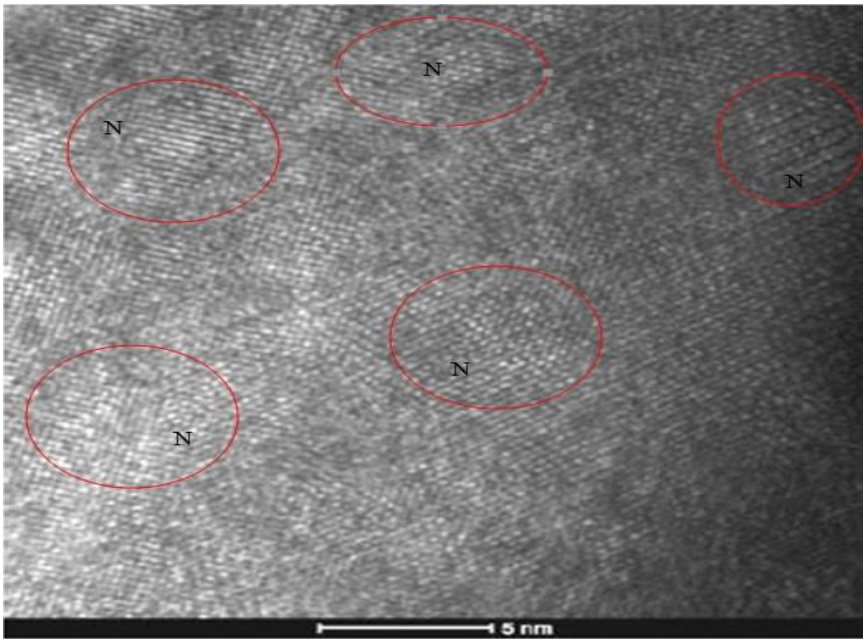

Figure 15: A typical HRTEM image with identified nanocystalline precipitates (N domain). In figure it is seen that the nanocrystallites and same crystal orientation as the precipitates in the different region (magnification X 1.5 000 000).

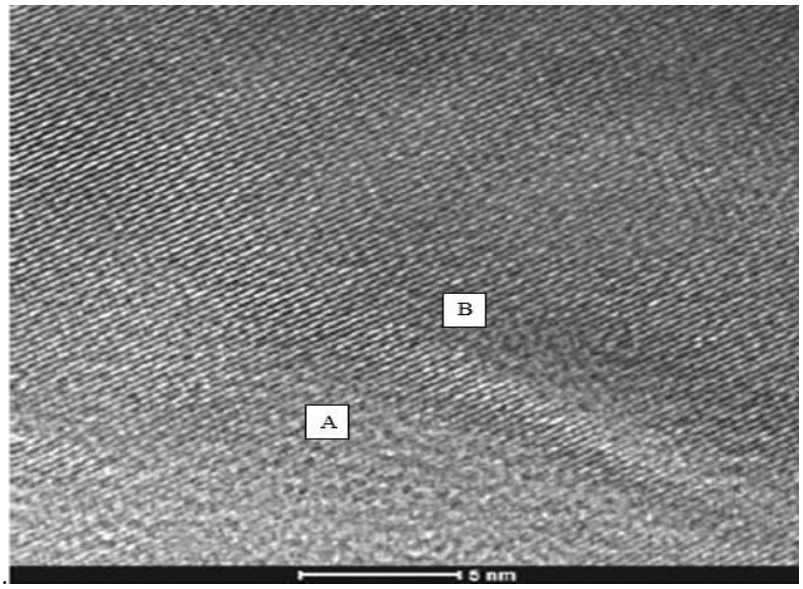

Figure 16: HRTEM image of nano-areas including images showing an interface (A-B) between nano-precipitates in the HEA on surface crystallization (magnification X 1.5 000 000).

3.2.1.2 Sample HVOF-HEA2-HT2

A photograph of the embedded cross-section of specimen HVOF-HEA2-S2-HT2 after exposure is depicted in Figure 17.

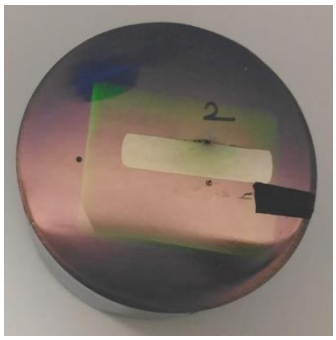

Figure 17: Cross-section through the HVOF-HEWA2-HT2 deposition

Corresponding SEM micrographs are reported in Figure 18 at low (a) and high (b) magnification.

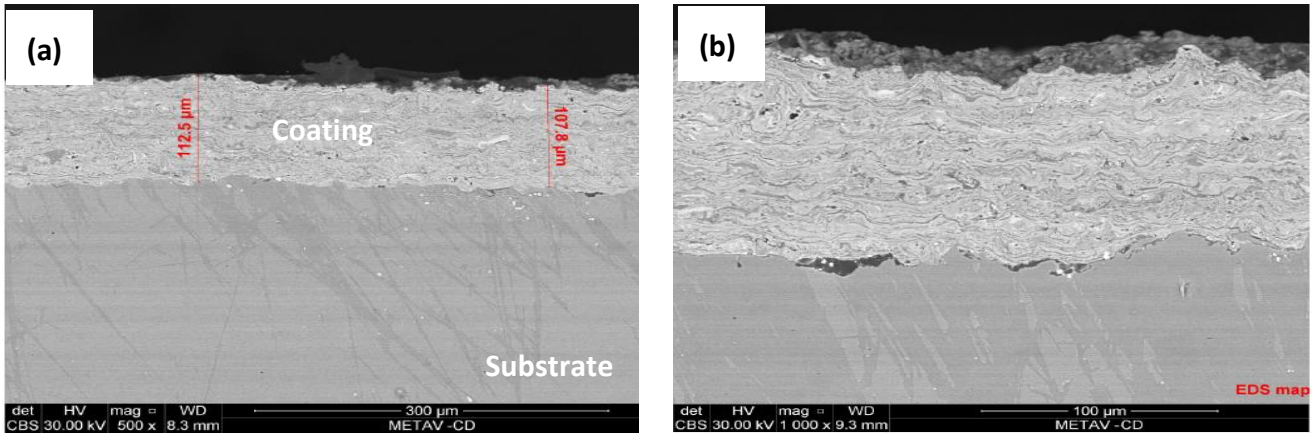

Figure 18: SEM micrographs showing sample HVOF-HEA2-HT2 in cross section.

The Figure shows a microstructure slightly different from what observed in the non heat-treated sample (Figure 9(b)), with the clear presence of phases of different composition, generated by the heat treatment process. Moreover, a thicker and denser corrosion film than what observed in specimen HVOF-HEA2 non heat-treated is observed at the surface of the coating. It is possible that the lower corrosion rate measured for this specimen is due to the barrier properties of this film.

In order to investigate further, EDX mapping of the specimen in Figure 18(b) has been performed (Figure 19). The analysis shows that the scale layer is mainly composed of the elements Cr, Co and Fe, with the former more abundant than the others. Clearly, thermodynamics have again favoured the formation of Cr-based corrosion products, which resulted in a thick barrier to the corrosion of the underlying coating.

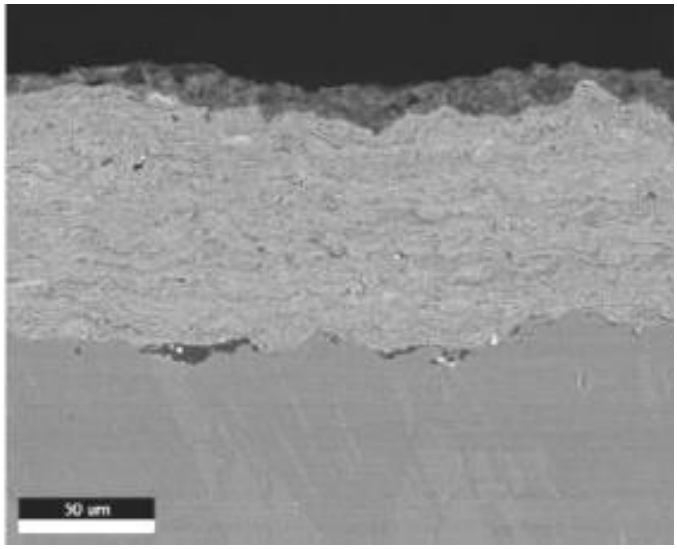

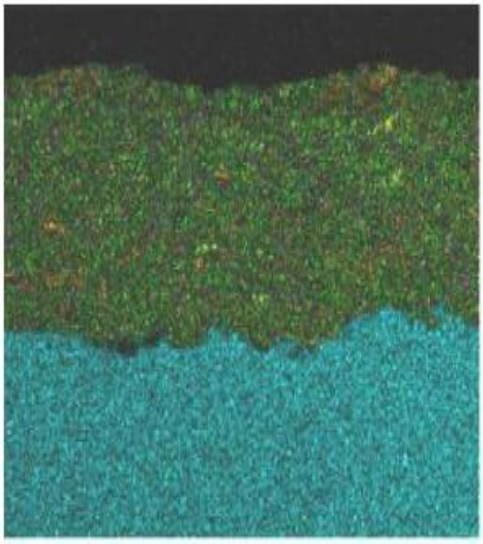

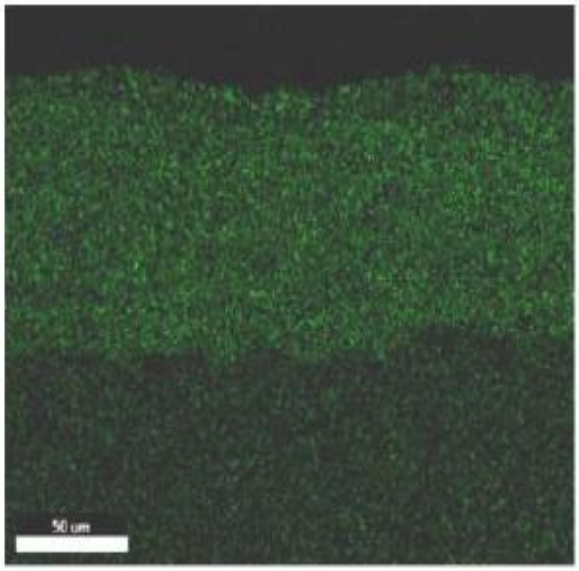

Co

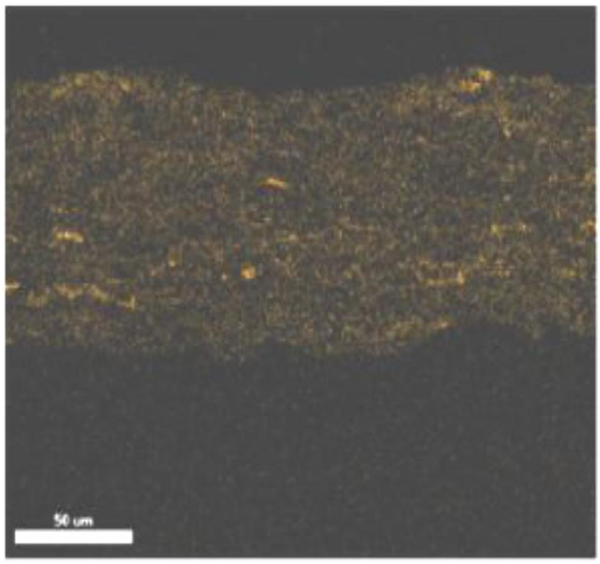

Cr

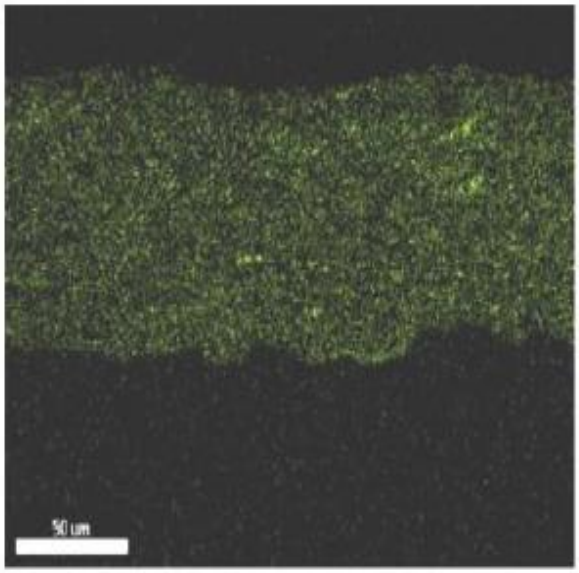

Ni

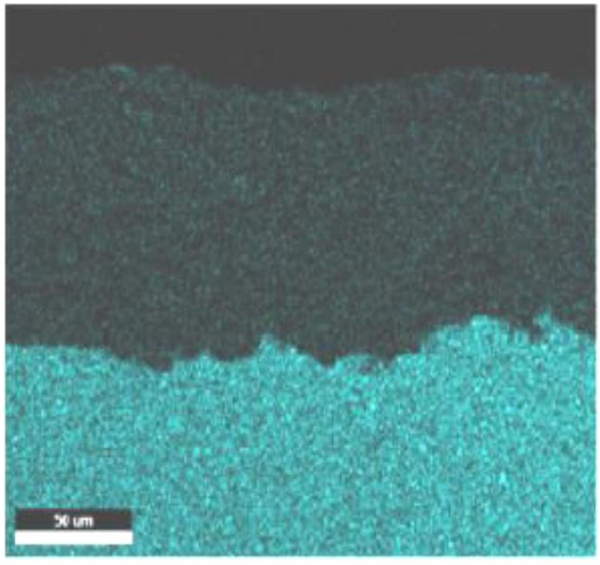

Fe

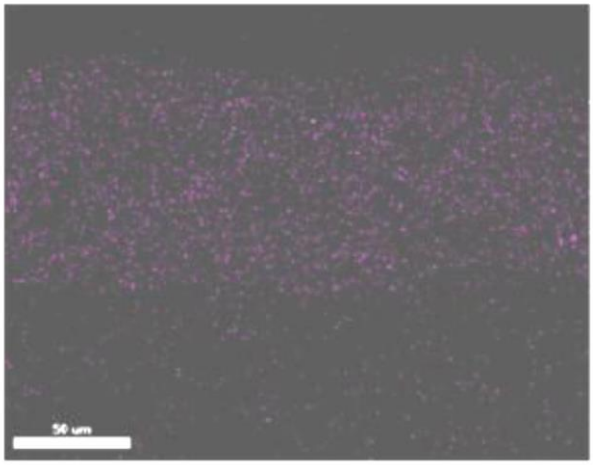

Figure 19: SEM-EDX analysis showing X-ray mapping for HEA elements and identification of disperse deposition of elements.

Further analysis has been performed in order to characterise, through TEM analysis, the details of the corrosion layer. The approximate location of TEM lamella selection is depicted in Figure 20. The resulting TEM micrograph is reported in Figure 21.

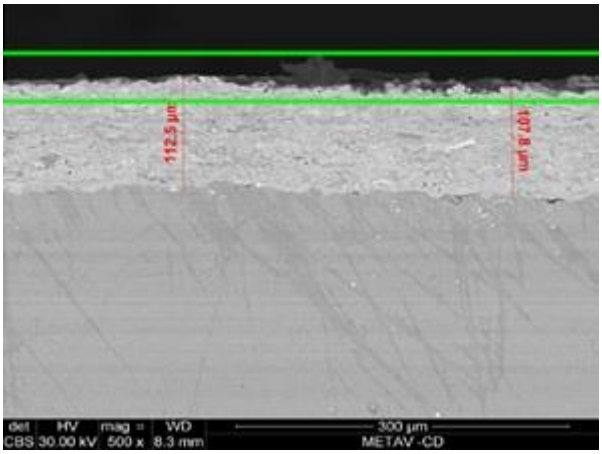

Figure 20: SEM micrograph showing the HEA deposition sample in the cross-section and indication of area for TEM sample preparation.

The HEA alloy shows the presence of micro precipitates (15 -20 nano-sized crystals with a round-like morphology) after heat treatment.

The morphology of these oxide scales, identified as rich in Cr, F, Mo and O, can be appreciated, at high magnification, in Figure 22 (TEM micrograph) and Figure 23 and 24 (SEM-EDX analysis).

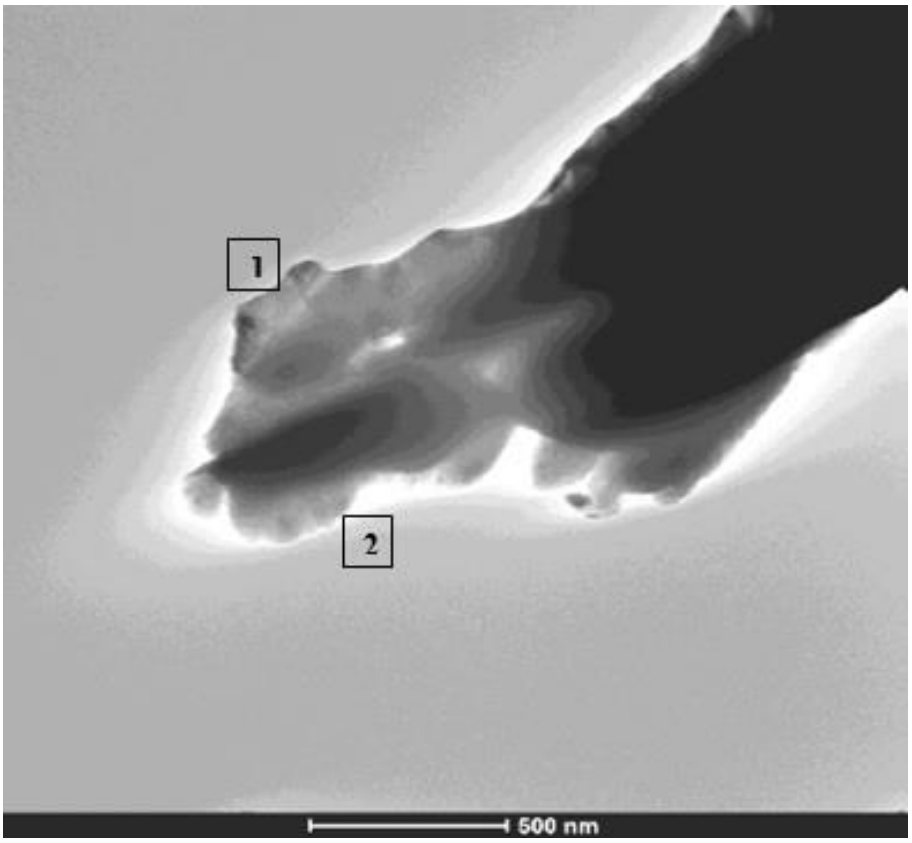

Figure 21: TEM micrograph of HVOF-HEA-HT2 layer after heat treatment state. The HEA alloy forming some micro precipitate (see area 1 and 2 in figure).

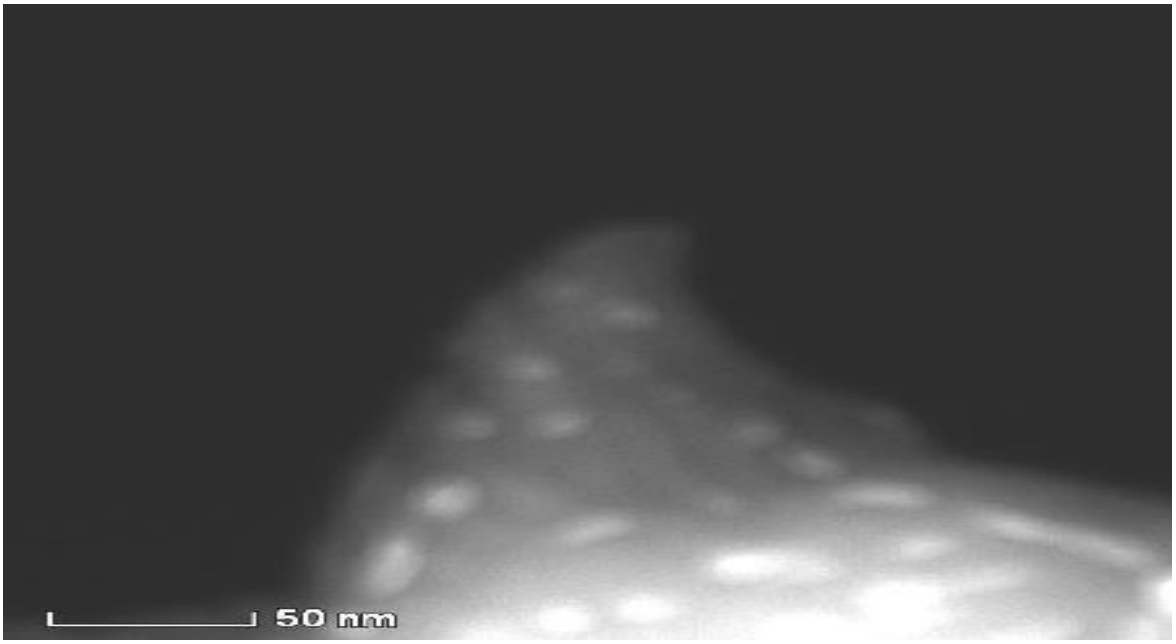

Figure 22: TEM micrographs showing Ni-Co-Mo nano-precipitates in specimen HVOF-HEA2-HT2.

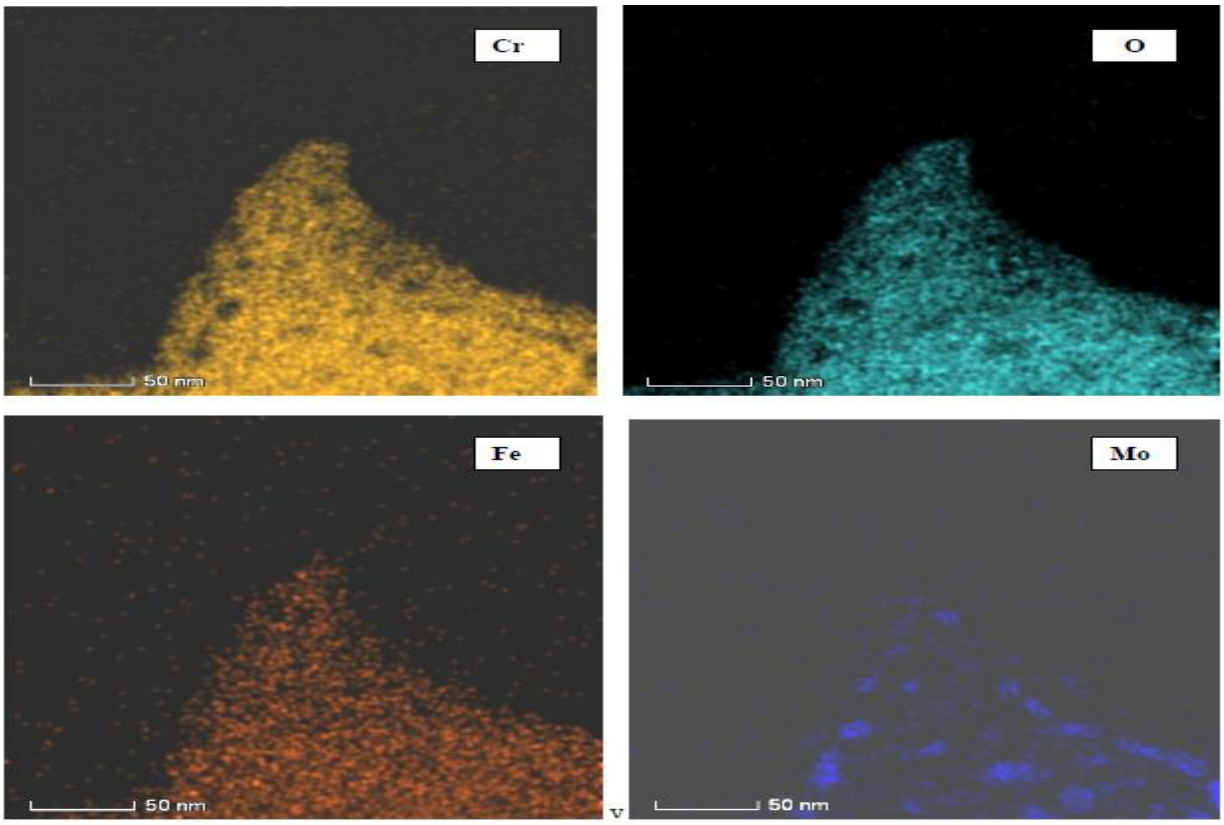

Figure 23: TEM mapping of HEA treated specimen showing the element distributions. Note a local area distribution of Mo particle with high matrix content of Cr and Fe.

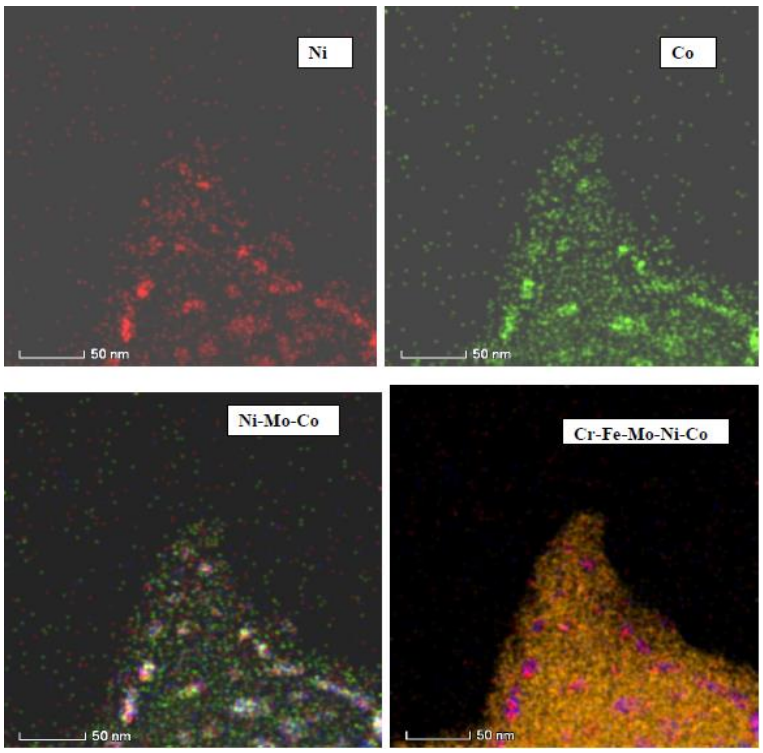

Figure 24: TEM mapping of HEA treated specimen showing the element distributions. Note a local area distribution of Ni-Co particle with complex HEA matrix.

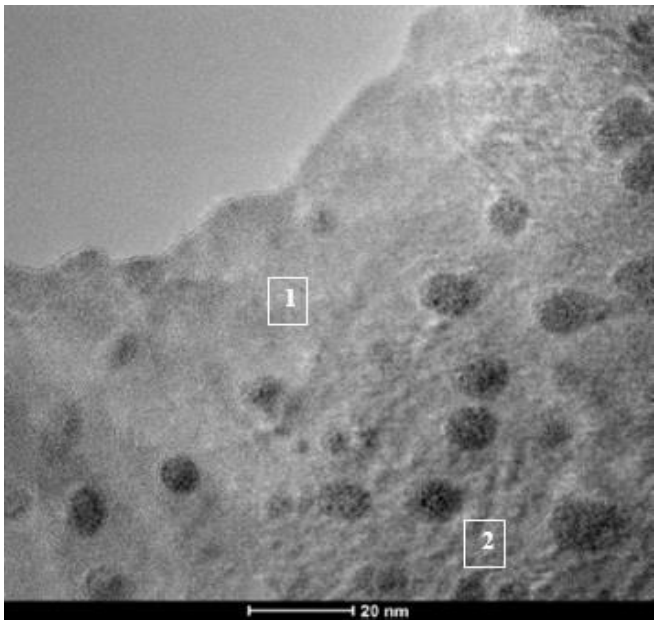

Figure 25: HRTEM image of nano-areas including nanostructure observed after treatment. There is an increase in nanoprecipitates Ni-Co_Mo (1) and the micrograph showing inadaptable dislocation network (2) shearing no special orientation in the matrix (magnification X 800 000).

The HRTEM micrograph (Figure 25) indicates that the precipitates in the HEA samples are more coherent with the matrix in the area (1) with particles of dimensions <10 nm. The lattices of HEA matrix are semi-coherent as can be seen from Figure 26. The lattice planes are continuous across the precipitate interface, except for a few, which end as a dislocation in area (2).

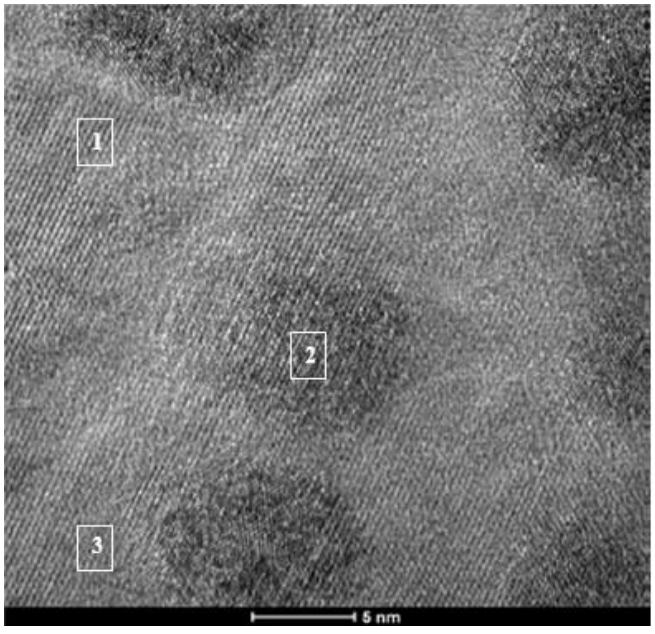

Figure 26: HRTEM image of nano-areas including images of homogeneity in the HEA crystallization (1) and structure nanoprecipitate (2) and dislocation networks (3) as response of the terminal treatment of samples (magnification X 1.5 000 000)

A complicating factor in HEA alloys that contain a large volume of Cr-Ni fraction, is the uniformity of the compositions of the matrix and the synergistic effect of Co and Mo. The solubility of different species in the matrix is a function of the HEA alloy content and the temperature. Some Cr-nano-precipitate were detected at each interface, which could block coating columnar grain growth and the oxidation of the matrix. It is therefore impossible to produce continuum and single-layer chromium oxide coating in the HEAs matrix.

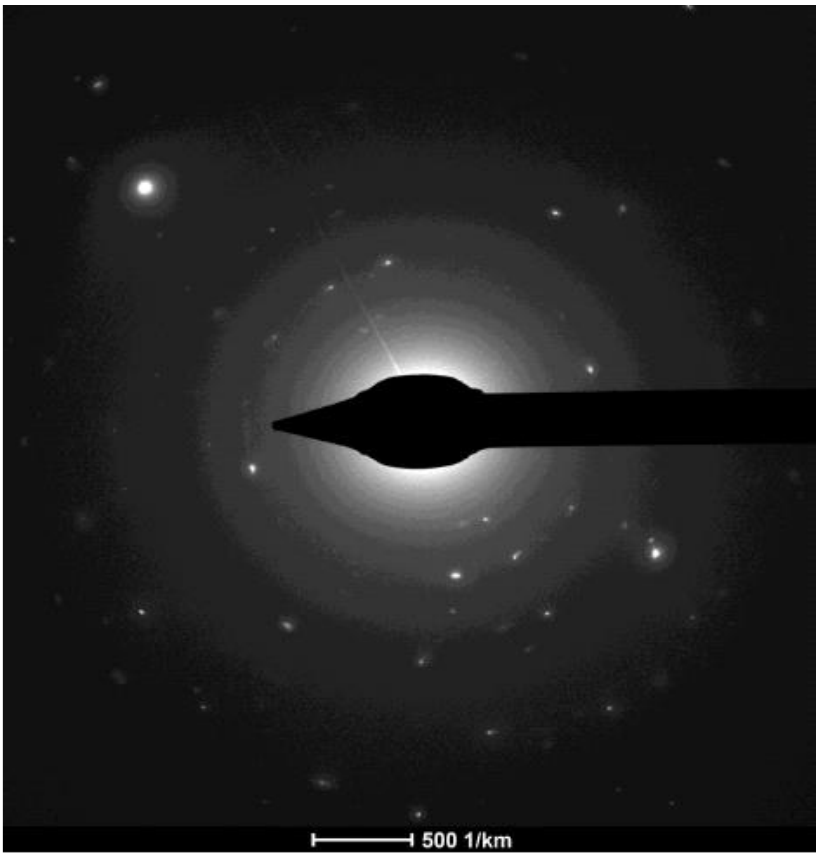

Figure 27: The diffractogram of a HREM image for the HEA sample.

The particles in Figure 25 and Figure 26 are compared. After heating treatment, the specimen have a different atomic arrangement, based on a detailed analysis on these micrographs. The analysis of the inter-atomic distance, leads to different structural models for the nanoparticles of specimen. It is very likely that the Co-Ni-Mo content varies in the different precipitates, in particular for the treated samples and that the Fe element is possible substituting to the elements Co or Ni or Mo in the final precipitates, because the oxygen is locate by Cr in the oxidation phenomena. The tendency for a metal to oxidize, like any other spontaneous reaction, is indicated by the free energy change ΔG accompanying the formation of the oxide. Most metals readily oxidize because ΔG is negative for oxide formation. The free energy released by the combination of a fixed amount of the oxidizing agent with the metal is given by ΔG_0 and is usually termed the standard free energy of the reaction. For this experimental HEAs the nucleation of Cr_2O_3 is favoured by higher Cr levels, higher temperatures and by HEA technique type of deposition. Once Cr_2O_3 is formed, if this film is removed or disrupted, then spinel oxidation is favoured because of the local lowering of Cr. Nevertheless, the significant presence of Cr-based oxidation products in this specimens seems to favour its corrosion resistance in respect to the non-heat-treated specimen.

3.2.2 LASER CLADDING COATINGS

3.2.2.1 SAMPLE LC-HEA2 (NON HEAT-TREATED)

The photograph of the LC-HEA2 (non heat-treated) specimen post exposure is depicted in Figure 28.

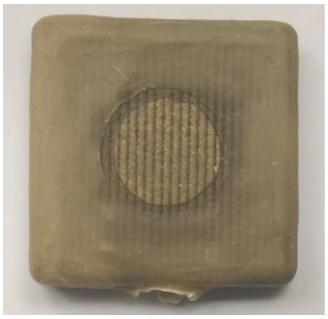

Figure 28: Cross-section through the LC deposition

A thickness up to 650µm dip deposition were achieved, characterized by a very fine dendrite structure and a highly regular interface with the steel substrate showing a very low dilution and strong adhesion (Figure 29). This high density has proven beneficial, for this particular alloy, to provide the coating with good corrosion and erosion-wear resistance within the project.

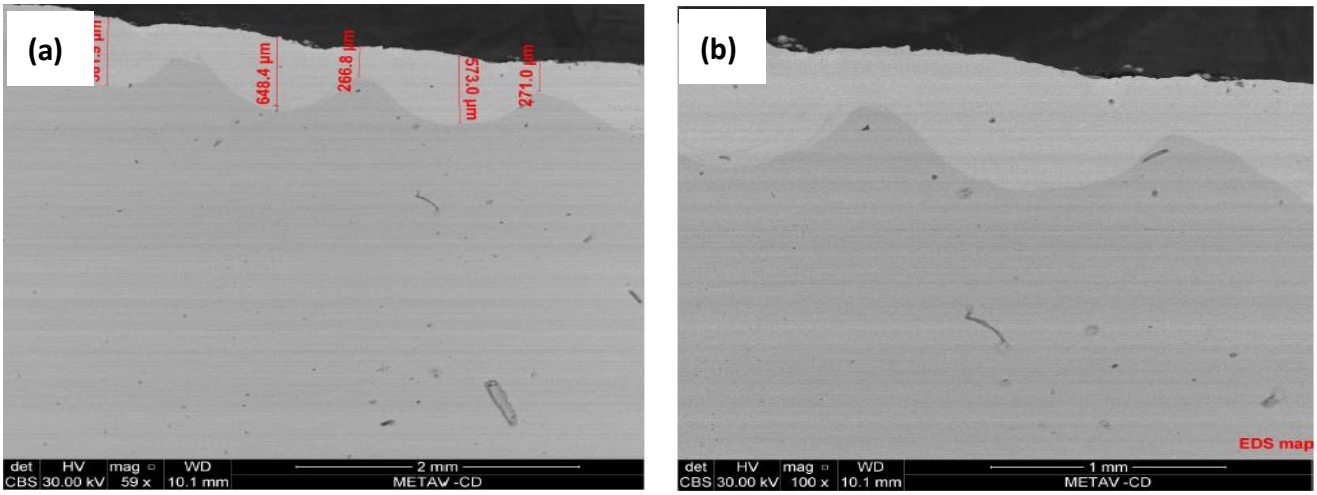

Figure 29: SEM micrographs showing the LC-HEA2 sample in cross section.

The laser processing and the cladding parameters are designed in such a way as to ensure that slight interdiffusion occurs only in the transition zone, in order to produce a metallurgical bond between base and the additional HEA component. The degree of intermixture and the percentage of base material in the layers is minimal (Figure 30). The EDX analysis further shows that a top layer, is present, rich in chromium is present, likely generated during exposure to the corrosive medium.

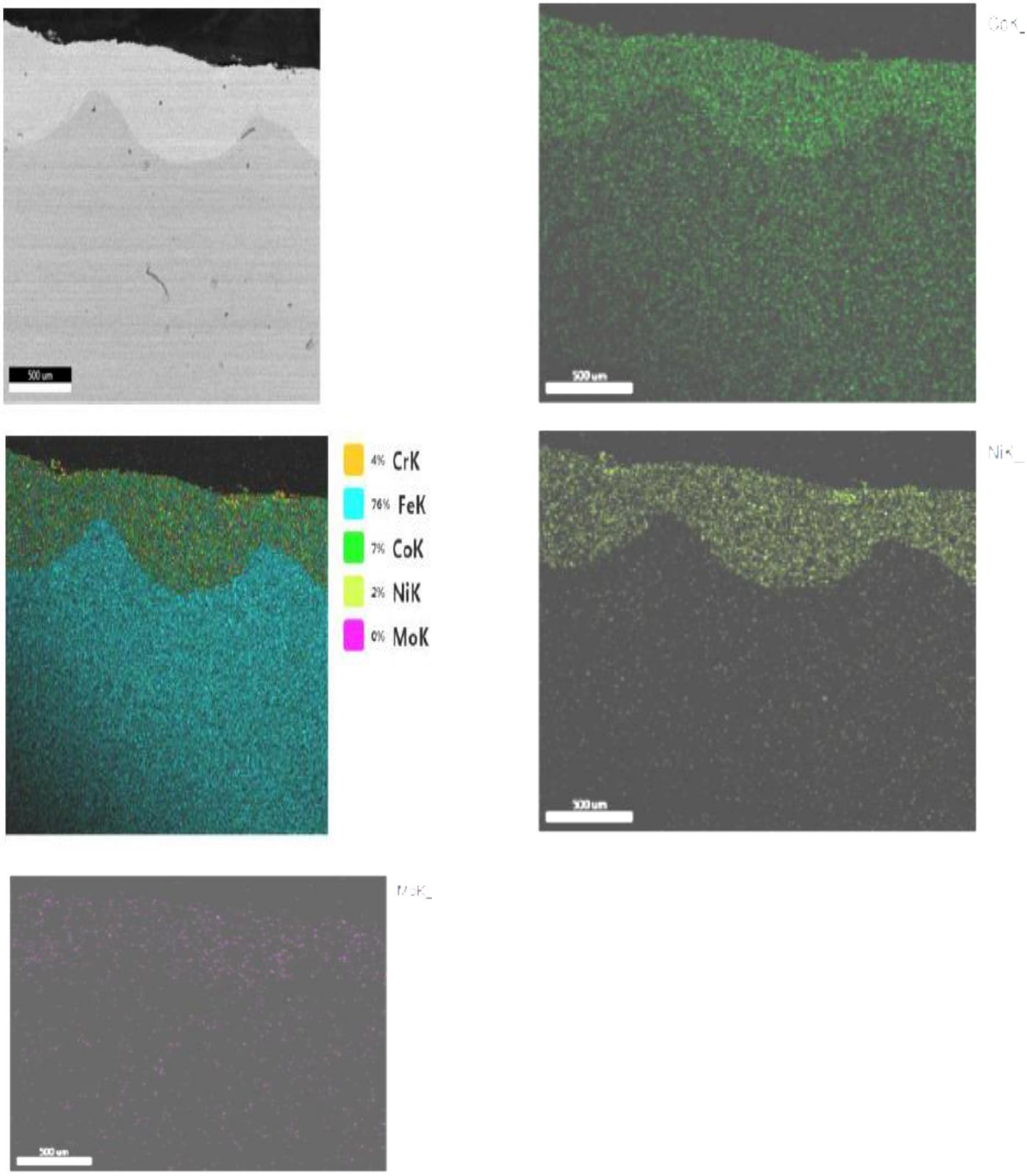

Figure 30: SEM and EDX general analysis showing X-ray mapping for HEA elements and identification of disperse deposition of elements.

A detailed microstructural analysis of the clad shows that it consists of some FeCrNi primary columnar dendrites and large areas of eutectic composed of FeCoNiCrMo and some HEA substructures in the interdendritic regions (no carbides from EDX identification). The FeCrNi

dendrites grow epitaxial, from the molten substrate and dissolve a large amount of iron, chromium and molybdenum. The results of the laser cladding coatings are presented in Figure 31.

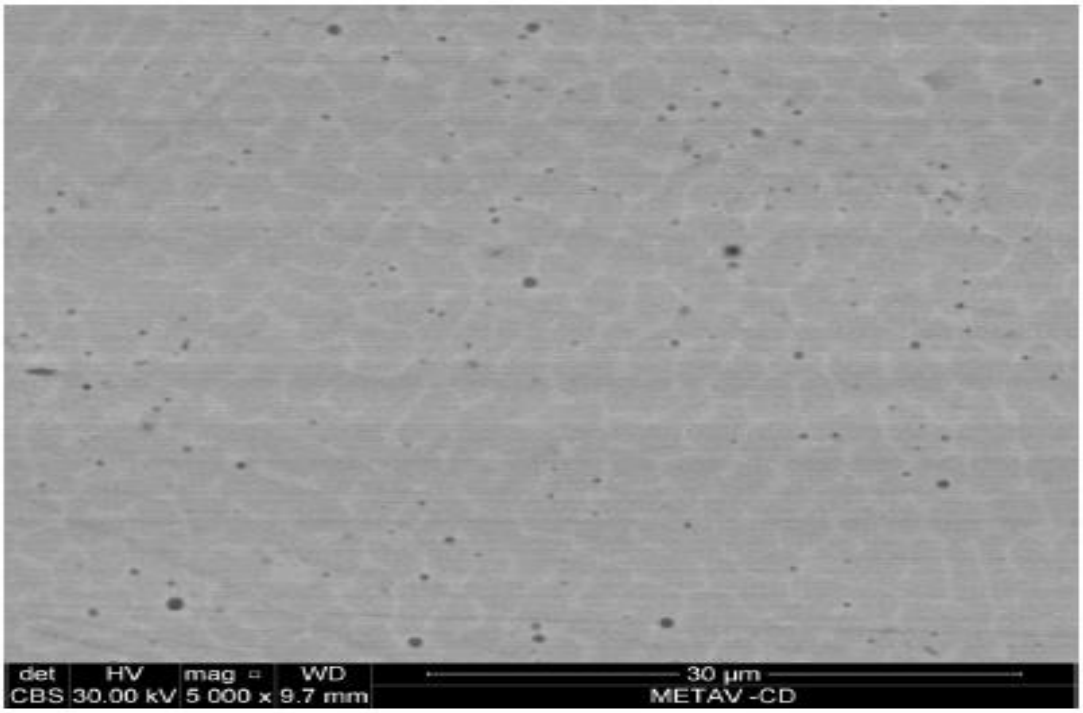

Figure 31: SEM backscattered image showing the microstructure of the clad LC-HEA2 alloy.

Further TEM analysis is performed in an attempt to identify the nature of the top layer. The location of lamella extraction is depicted in Figure 32.

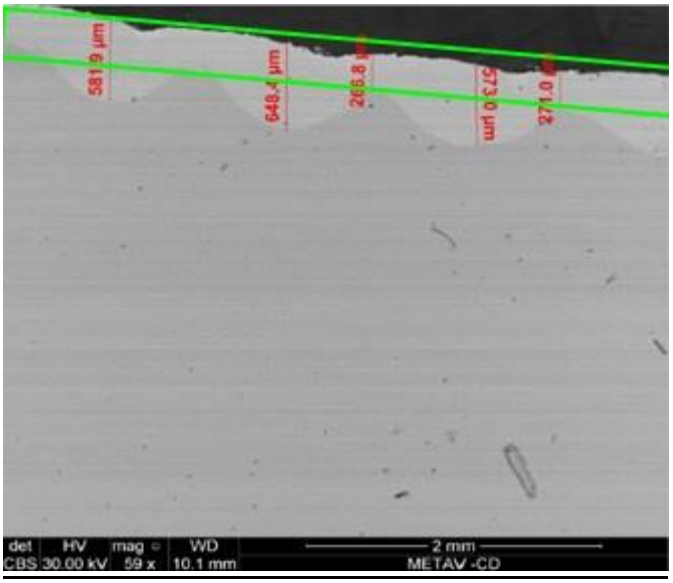

Figure 32: SEM micrograph showing the LC-HEA2 sample in the cross-section and indication of area for TEM sample preparation.

TEM micrographs for the products from the diffusion HEA alloy area are presented in Figure 33, with the respective diffraction patter shown in Figure 34.

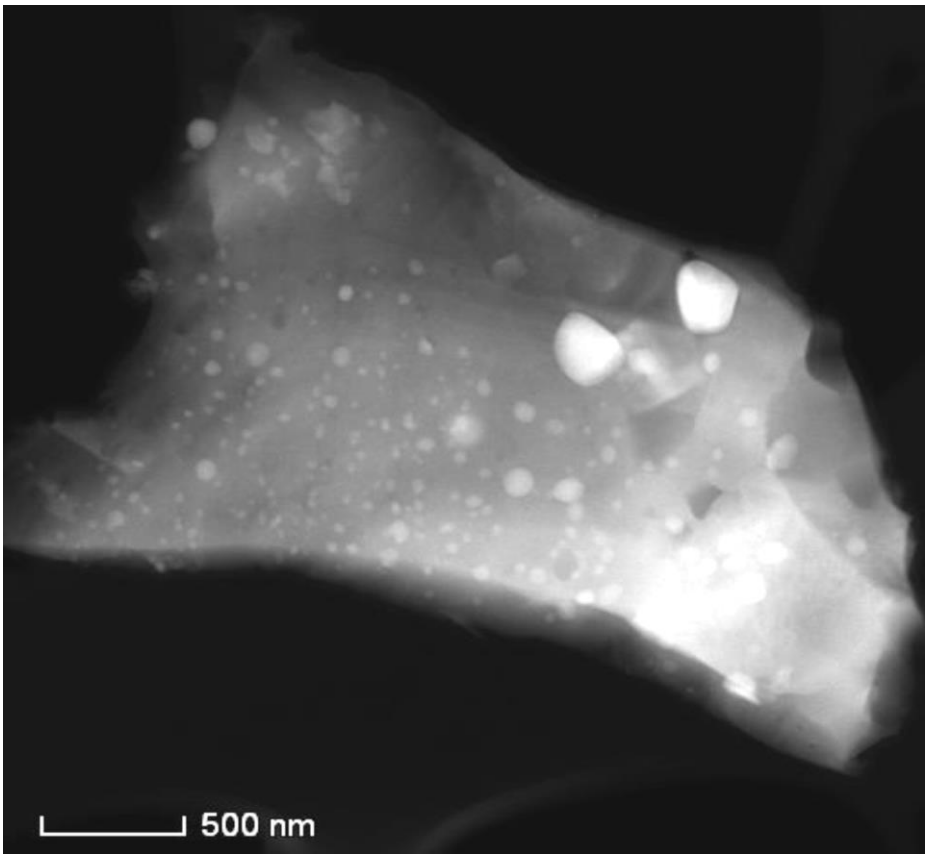

Figure 33: TEM micrograph of LC-HEA2 top layer at non treated state.

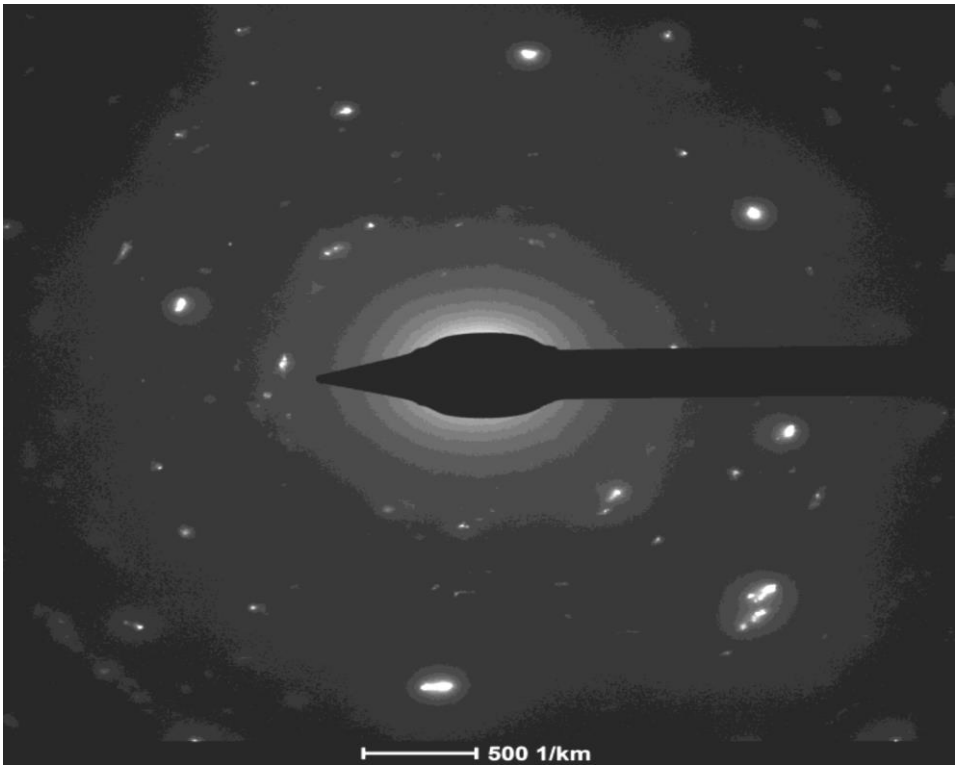

Figure 34: TEM Electron diffraction pattern show some microcrystals format as surface of deposition of HEA laser layer.

Isolated spots are caused by diffraction in a few small isolated grains where the transformation to the surface layer primary-oxidation in laser deposition. EDX mapping (Figure 35) shows elements not uniformly distributed within the HEA alloy, with significant presence of Cr and O elements. Silicon is also probed in the region, likely due to the lacquer used to protect the un-tested areas of the specimen during exposure (see Figure 28).

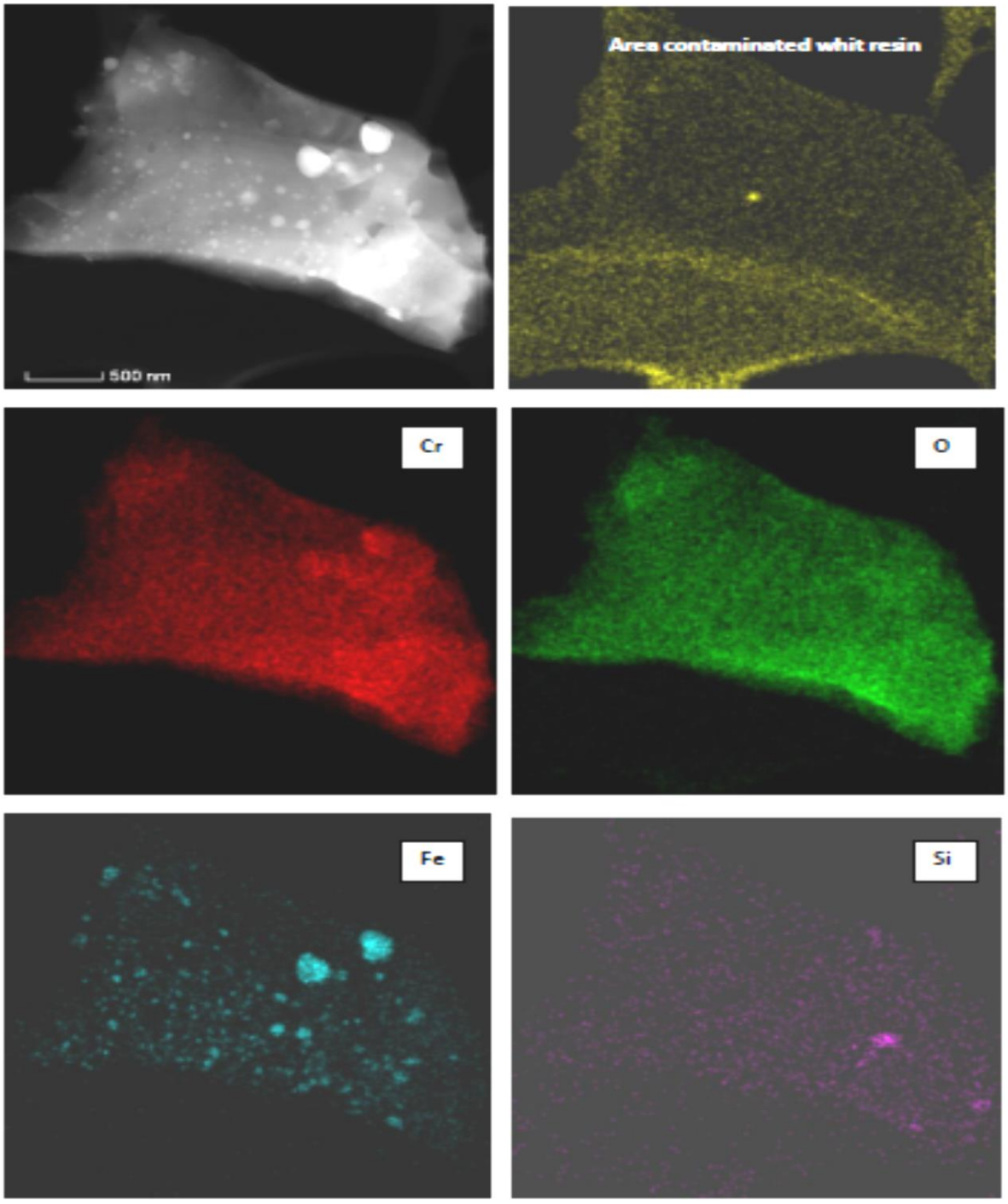

Figure 35: TEM-EDX mapping of HEA treated specimen showing the element distributions (Cr, O, Fe, Si) and the contaminated area with resin.

3.2.2.2 SAMPLE LC-HEA2-HT2

A photograph of the exposed surface of specimen LC-HEA2-HT2 is depicted in Figure 36.

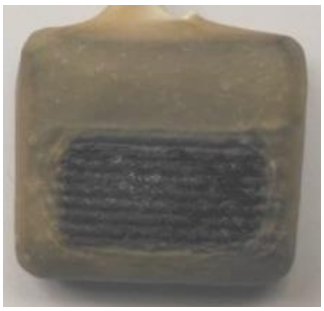

Figure 36: Surface photograph of specimen LC-HEA2-HT2 after exposure.

Again, as for what observed in specimen LC-HEA2 (non heat-treated) a dense microstructure with no apparent presence of defects is observed. However, a much thicker scale than what observed in Figure 29(b) is shown on the top surface of the specimen. The scale does appear to be porous, which suggests that it would not perform well as a barrier to the corrosion solution.

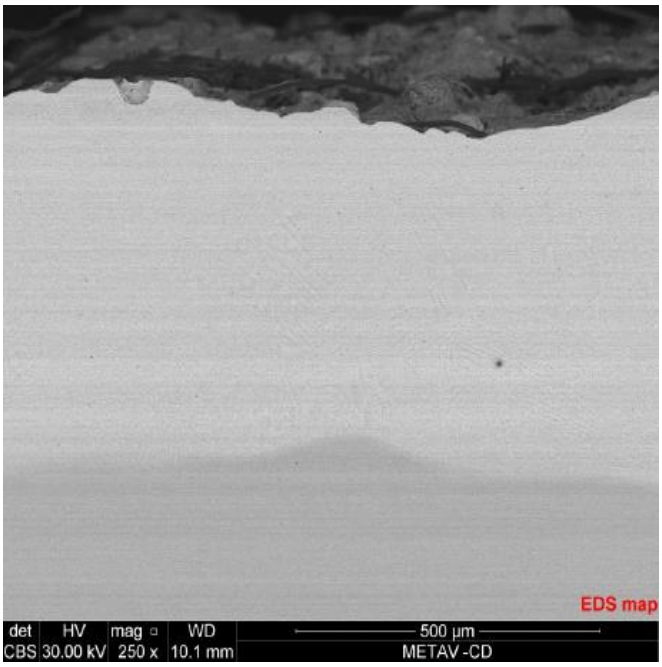

Figure 37: SEM micrograph showing the cross-section of specimen LC-HEA2-HT2 after exposure.

SEM-EDX mapping of the SEM micrograph (Figure 38) shows that the top layer contains all of the components of the HEA2 alloy, with dominance of Cr, thus again suggesting the formation of Cr-based oxides.

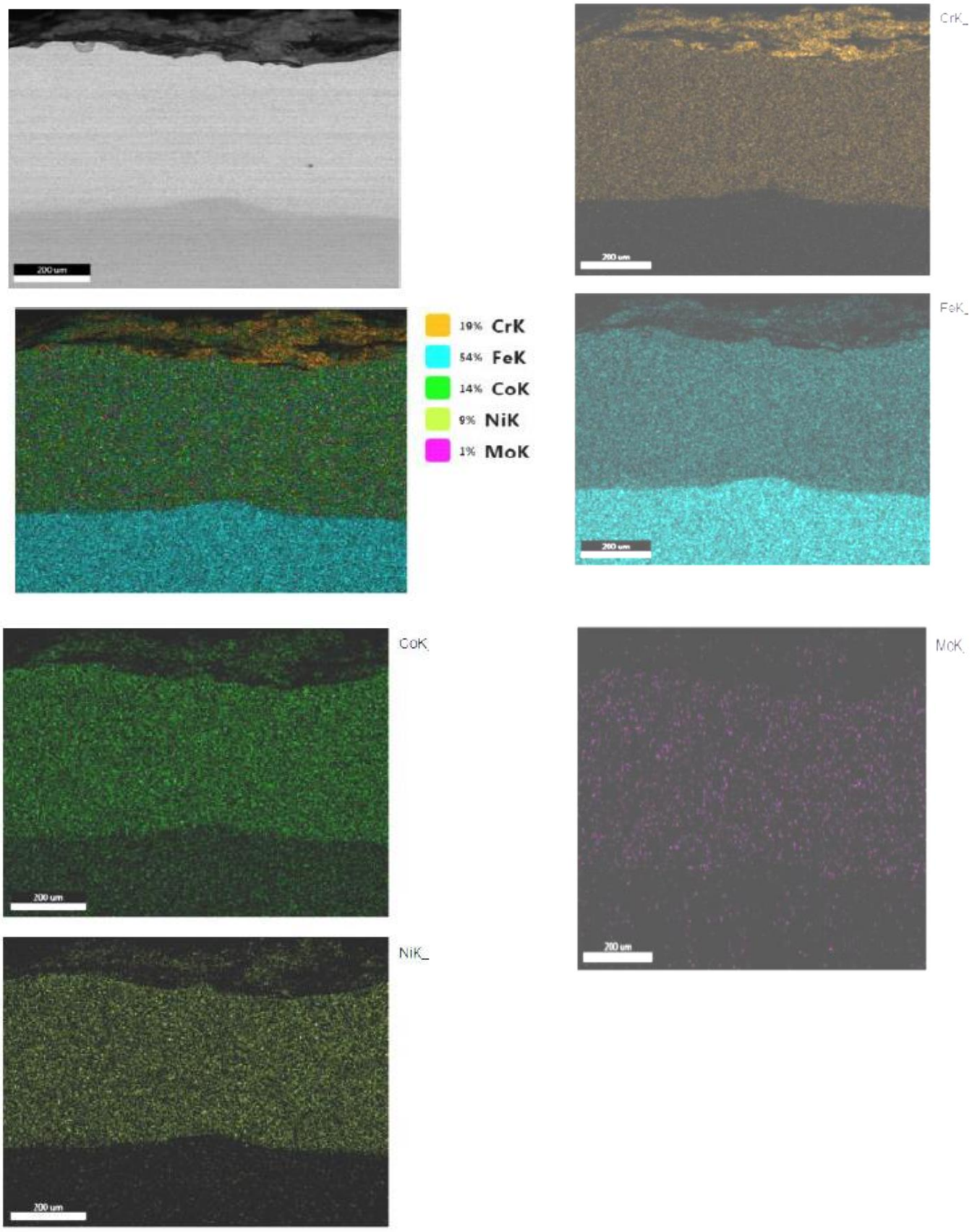

Figure 38: SEM and EDX general analysis showing X-ray mapping for LC-HEA2-HT2 elements and identification of disperse deposition of elements.

Details on the microstructure of the laser clad microstructure can be found in Figure 39. The structure formed of laser heat threated specimen deposition consist of FeCrNi primary columnar dendrites and large areas of eutectic composed of FeCoNiCrMo and some HEA substructures in the interdendritic regions (no carbides in the EDX identification). The FeCrNi dendrites grow epitaxial, from the molten substrate and included iron, chromium and molybdenum elements.

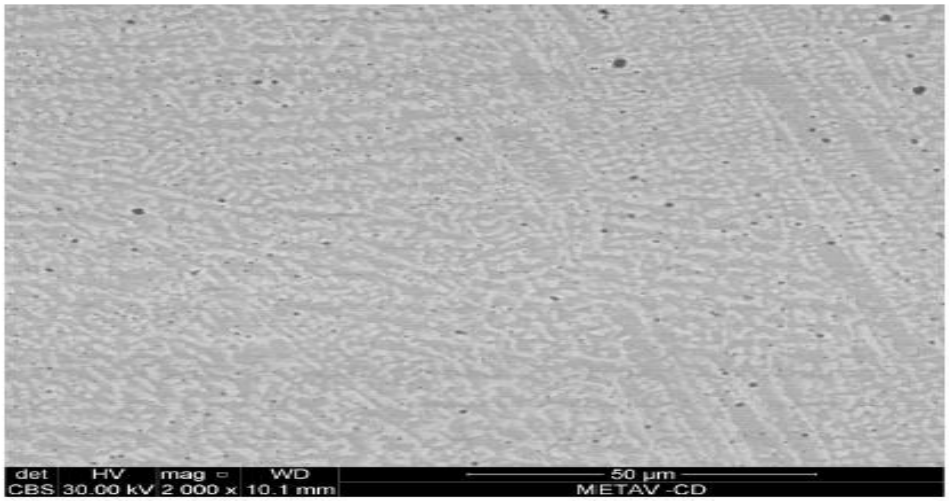

Figure 39: Back scattering image (CBS) for composition of LC-HEA2-HT2 alloy on the coating. Aspect of the general microstructure of the clad HEA treated alloy on coating.

A more in-depth analysis on the nature of the corrosion film at the surface of the coating can be performed by TEM. The region selected for the extraction of the TEM lamella is depicted in Figure 40.

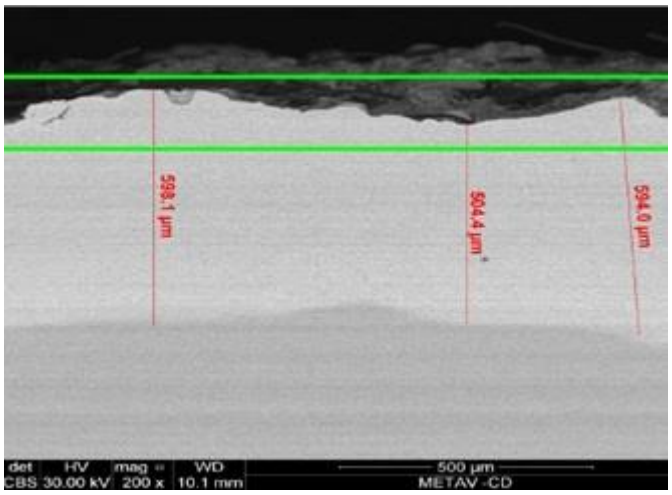

Figure 40: The micrograph shows the LC-HEA2 sample in cross-section and indication of the area for TEM lamella preparation.

The TEM micrograph of a region identified in the coating is reported in Figure 41.

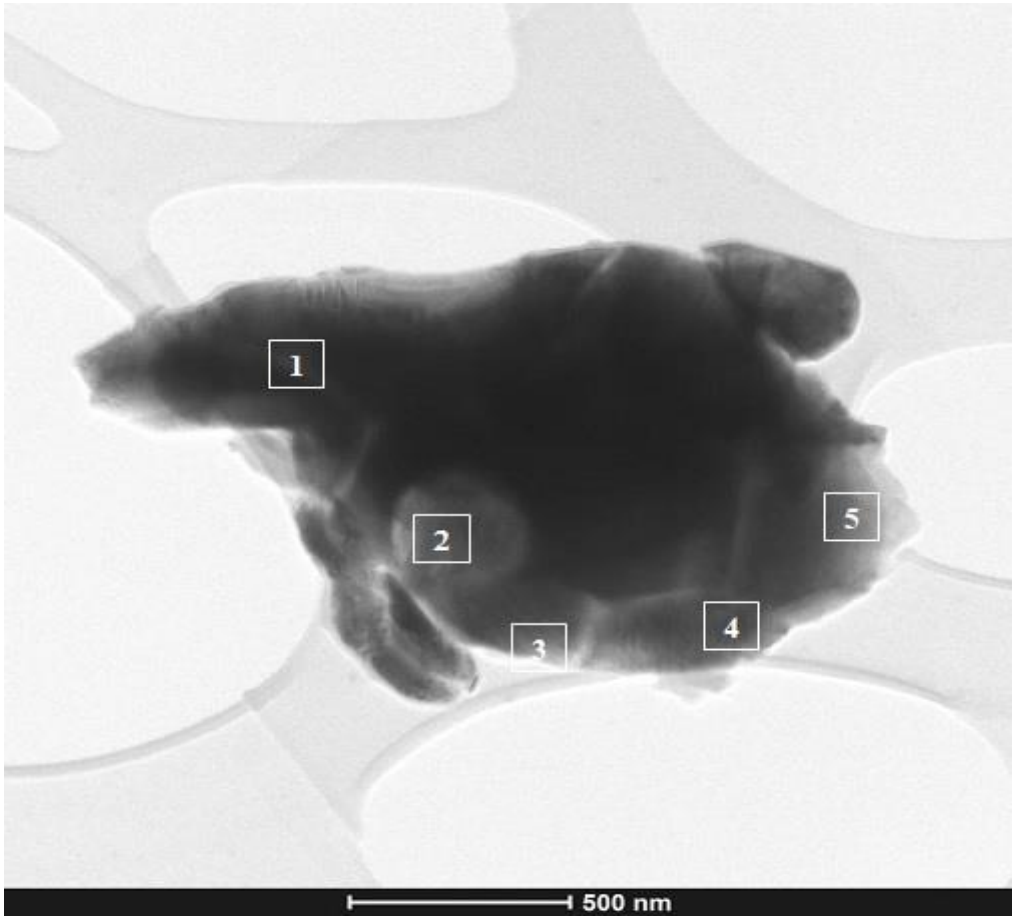

Figure 41: TEM micrograph of LC-HEA2-HT2 top layer.

The alloy seems to form micro precipitates (1-5 micron sized crystals with a polygonal-like morphology as identified in the figure) after heat treatment. The Selected Area Diffraction Pattern (SAED) of the micrograph in Figure 41 is reported in Figure 42.

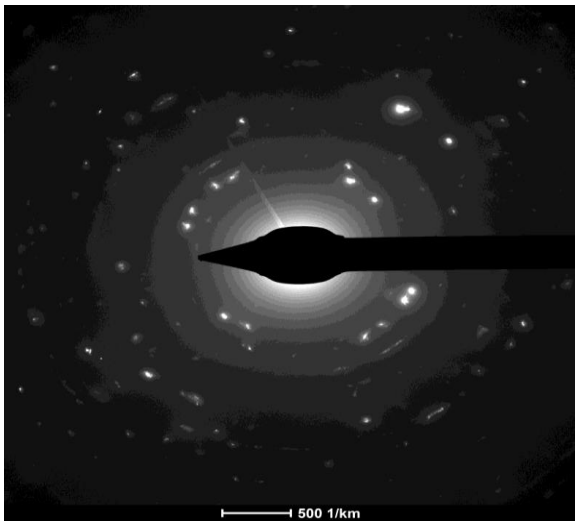

Figure 42: Selected area diffraction patterns (SAED) of deposition show the presence some rings from the fine grained Cr_2O_3 particle formatted as surface deposition of LC-HEA2-HT2 layer.

Some isolated diffraction points, caused by diffraction in a few small isolated grains, are observed. Supplementary rings also appear, caused by the supplementary oxide on surface layer on the end of heat treatment.

Elemental distribution image showing elements distribution of HEA alloy and also shows the effect of carbon coating/ resin in contaminated area of sample are depicted in Figure 43. It is likely that high contamination caused by the polymeric lacquer used to protect the un-coated areas of the specimen from corrosion have been preferentially observed in the TEM analysis, thus affecting the results.

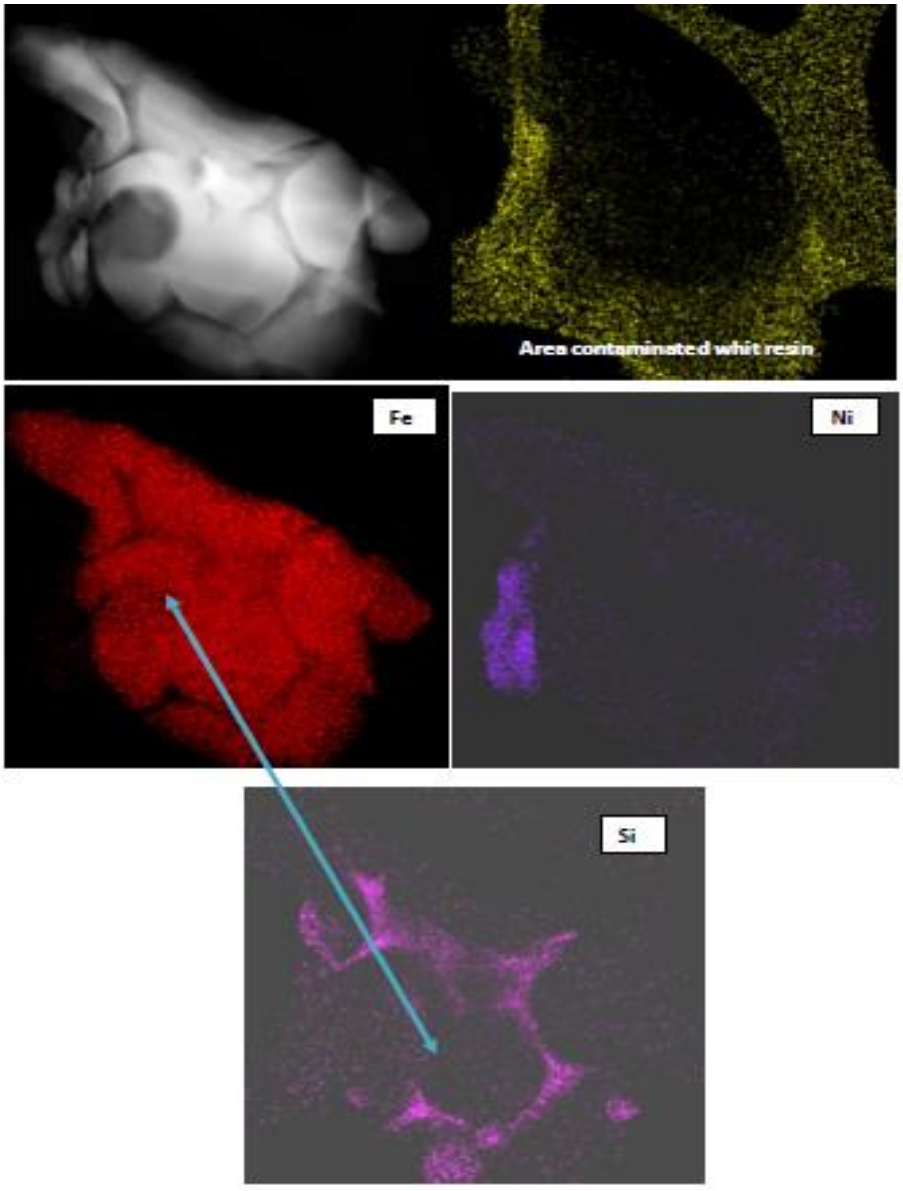

Figure 43: TEM mapping of LC-HEA2-HT2 specimen showing element distributions (Fe, Ni). Note a inter crystalline Si particle with high content of Si possibly due by contamination by the lacquer employed to protect the un-coated areas of the specimen from corrosion.

4. CONCLUSIONS

In this work, High-Entropy Alloy (HEA) coatings, deposited by High-Velocity Oxygen Fuel (HVOF) and Laser Cladding (LC) have been tested, by linear polarisation resistance in an acidic chloride-containing solution, in the as-deposited and heat-treated conditions in order to assess the influence of passive film. Two heat treatment conditions, HT1 (900^{o}C) and HT2 (1100^{o}C) have been employed.

The work has highlighted the main following findings:

- The heat-treatment has a positive effect onto the corrosion behaviour of HVOF coatings, possibly due to the formation of a dense passive film on the exposed surface of the coating. A more porous and thinner film is in fact observed on the surface of the non-heat treated specimen.
- The heat treatment has a negative effect onto the corrosion behaviour of LC coatings. The thick film observed on the surface of the exposed heat-treated coatings shows high level of porosity, while a much denser film is present on the surface of non heat-treated specimens.
- The passive film formation seems to be dominated by the Cr element, although other components of the HEA (i.e. Co, Ni, Fe and Mo) are generally also detected.

REFERENCES

[1] Sturgeon, A.J., Perrin, C., McCartney, D.G.: Development of Thermal Sprayed Plain Bearings for Automotive Engine Applications. In: Surface Engineering & Tribology for Future Engine and Drivelines Conference, London, 16-22, 2006;

[2] J. Mazumder, “1 - Laser-aided direct metal deposition of metals and alloys,” Materials, Design, Technologies, and Applications, no. Woodhead Publishing Series in Electronic and Optical Materials, 21-53, 2017;

[3] Wall JS; Hainfeld JF (1986). "Mass mapping with the scanning transmission electron microscope". Annu Rev Biophys Chem. 15: 355–76.doi:10.1146/annurev.bb.15.060186.002035.PMID 3521658;

[4] P.J. Goodhew, “Final thinning: ion beam thinning and mechanical techniques” in Thin Foil Preparation for Electron Microscopy”, Elsevier, 1985;

[5] D.B. Eilliams , C.B. Carter, “ Specimen Preparation” in Transmission Electron Microscopy: A textbook for Materials Science, Plenum Press, New York, 1996;

[6] L. Reimer;R. Kohl, “Transmission Electron Microscopy Physics of Image Formation”, Springer, 2008, ISBN 978-0-387-40093-8;

[7] Xu, Peirong; Kirkland, Earl J.; Silcox, John; Keyse, Robert "High-resolution imaging of silicon (111) using a 100 keV STEM", Ultramicroscopy, 32 (2): 93–102, 1990.